



## Observations of drifter dispersion in the surfzone: The effect of sheared alongshore currents

Matthew S. Spydell,<sup>1</sup> Falk Feddersen,<sup>1</sup> and R. T. Guza<sup>1</sup>

Received 12 February 2009; revised 4 May 2009; accepted 6 May 2009; published 31 July 2009.

[1] Surfzone dispersion is characterized with single-particle Lagrangian statistics of GPS-tracked drifters deployed on 5 days at Huntington Beach, California. Incident wave heights varied weakly between days, and stationary rip currents did not occur. Generally, the time-dependent bulk surfzone cross-shore diffusivity  $\kappa_{xx}$  was similar on all days, reaching a local maxima of approximately  $1.5 \text{ m}^2 \text{ s}^{-1}$  between 160 and 310 s, before decreasing to about  $1 \text{ m}^2 \text{ s}^{-1}$  at 1000 s. The alongshore diffusivity  $\kappa_{yy}$  increased monotonically to 1000 s and was variable between the 5 days. For times greater than 30 s, the alongshore diffusivity is greater than the cross-shore diffusivity, consistent with previous observations. The observed diffusivities are fit to analytic functional forms, from which asymptotic diffusivities and Lagrangian timescales are determined. The asymptotic alongshore diffusivity  $\hat{\kappa}_{yy}^{\infty}$  varies between 4 and  $19 \text{ m}^2 \text{ s}^{-1}$ , and this variation is related to the variation in the maximum of the mean alongshore current  $\bar{v}_m$ , broadly consistent with a shear dispersion scaling  $\hat{\kappa}_{yy}^{\infty} \sim \bar{v}_m^2$ . Cross-shore variation in dispersion processes, lumped together in the bulk  $\kappa$ , is apparent in the non-Gaussian probability distribution function of drifter displacements at intermediate times (30 s). Both biased and unbiased diffusivity sampling errors depend on the number and length of drifter trajectories and limit aspects of the analysis.

**Citation:** Spydell, M. S., F. Feddersen, and R. T. Guza (2009), Observations of drifter dispersion in the surfzone: The effect of sheared alongshore currents, *J. Geophys. Res.*, *114*, C07028, doi:10.1029/2009JC005328.

### 1. Introduction

[2] Polluted water sickens beachgoers and significantly impacts coastal United States economies [Dorfman and Rosselot, 2008]. Polluted surfzone waters often have high levels of fecal indicator bacteria [Reeves *et al.*, 2004] and human viruses [Jiang and Chu, 2004]. Dilution and diffusion between the surfzone and offshore waters are believed to be the primary cause of (fecal indicator) *Enterococcus* bacteria inactivation [Boehm *et al.*, 2005]. Horizontal diffusion and dispersion must be understood to predict the fate of surfzone tracers, including pollution, plankton, and larvae.

[3] Tracer dispersion can be estimated from Lagrangian drifter data. The theory for single-particle (absolute) dispersion in homogeneous turbulence relates Lagrangian velocity statistics to the diffusivity [Taylor, 1921]. Diffusion is ballistic (i.e., linear diffusivity growth with time) at short times, and Brownian (i.e., constant diffusivity) at long times relative to the Lagrangian timescale. Davis [1987, 1991] developed the methodology for studying oceanic absolute diffusion including the effects of inhomogeneity. Surface and subsurface drifters have been used to directly estimate

the large-scale diffusivity of the oceanic general circulation [e.g., Lumpkin *et al.*, 2002], the California Current [Swenson and Niller, 1996], and continental shelf regions [e.g., Dever *et al.*, 1998]. Lacasce [2008] provides an excellent review.

[4] A goal of surfzone mixing research is to estimate the surfzone eddy diffusivity, which could be used in a Fickian diffusion equation for a surfzone tracer, and to determine the diffusivity dependence upon surfzone parameters such as wave height and mean currents. Surfzone diffusivity was first estimated by measuring the alongshore spreading rate of fluorescent dye tracer at the shoreline [Harris *et al.*, 1963; Inman *et al.*, 1971; Grant *et al.*, 2005; Clarke *et al.*, 2007]. Surfzone eddy diffusivity estimates varied considerably, in part because the single realization of a the observed tracer patch precluded the averaging necessary for statistically stable diffusivity estimates. More recently, GPS-tracked surfzone drifters [Schmidt *et al.*, 2003] have been used to study surfzone circulation and diffusion in the field. Drifters have been used to estimate absolute and relative diffusivities in rip-current dominated surfzone circulations [Johnson and Pattiaratchi, 2004; Brown *et al.*, 2009], and to observe rip currents and surfzone eddies on irregular bathymetry [Schmidt *et al.*, 2005]. Surfzone drifters have been included in wave-resolving numerical models of transient rip currents [Johnson and Pattiaratchi, 2006].

[5] Two days of drifter observations at Torrey Pines CA in 2004 (TP04 experiment) were used to estimate time-dependent absolute diffusivities [Spydell *et al.*, 2007]. On

<sup>1</sup>Integrative Oceanography Division, Scripps Institution of Oceanography, University of California San Diego, La Jolla, California, USA.

day one, wave heights were small and mean currents were weak, whereas on day two larger obliquely incident waves drove a strong alongshore current. On both days, initially the cross-shore diffusivity is larger than the alongshore diffusivity ( $\kappa_{xx} > \kappa_{yy}$ ) but, after many wave periods ( $\approx 100$  s),  $\kappa_{yy} > \kappa_{xx}$  [Spydell *et al.*, 2007]. That is, after initially more rapid cross-shore spreading, alongshore diffusion is faster than cross-shore diffusion. At the longest times studied ( $\approx 600$  s), diffusivities on day 1 ( $\kappa_{xx} \approx 0.75 \text{ m}^2 \text{ s}^{-1}$ , and  $\kappa_{yy} \approx 2 \text{ m}^2 \text{ s}^{-1}$ ) were smaller than on day 2 ( $\kappa_{xx} \approx 1.25 \text{ m}^2 \text{ s}^{-1}$ , and  $\kappa_{yy} \approx 4 \text{ m}^2 \text{ s}^{-1}$ ). However, as discussed by Spydell *et al.* [2007], this study was limited by the relatively short trajectory lengths on day two (on average  $\approx 500$  s), the day with large waves and strong alongshore currents, prompting the use of a biased Lagrangian velocity autocovariance estimator.

[6] The processes leading to time-dependent surfzone diffusivities (and hence dispersion) are not clearly understood. The TP04 day one (small waves) observed drifter dispersion was well modeled with numerical drifters seeded into a Boussinesq wave and current model [Spydell and Feddersen, 2009]. The dominant dispersion mechanism was surfzone macro vortices forced by finite-crest length breaking [e.g., Peregrine, 1998]. Irrotational surface gravity waves (sea swell or infragravity) motions had negligible dispersive capacity [Spydell *et al.*, 2007; Spydell and Feddersen, 2009]. Shear wave generated eddies [e.g., Oltman-Shay *et al.*, 1989] and shear dispersion [e.g., Taylor, 1953] may have contributed to the TP04 day two elevated alongshore diffusivity [Spydell *et al.*, 2007].

[7] Surfzone drifter observations and estimates of absolute diffusivities are still scarce, particularly on beaches without bathymetric controls on the circulation. GPS-tracked Lagrangian surfzone drifter data was collected at Huntington Beach CA on an alongshore uniform beach for five days with moderate waves and varying alongshore currents (section 2). Drifters were released mostly within the surfzone and drifters typically stayed within the surfzone with trajectory lengths between 15 and 30 min. Relative to prior work [Spydell *et al.*, 2007], longer trajectories allow for longer and more stable diffusivity estimates. The observed Lagrangian statistics are presented in section 3. Unbiased Lagrangian velocity autocovariance functions are used to estimate diffusivity and dispersion (section 3.1). The observed diffusivities are fit to analytic functional forms from which asymptotic values and Lagrangian timescales are determined (section 3.2). Analogous to the open ocean [Gille and Llewellyn Smith, 2000; LaCasce, 2005], the nondimensional probability distribution function (pdf) of Lagrangian displacements is estimated and the degree to which the pdf is non-Gaussian is assessed with the Kolmogoroff-Smirnoff (K-S) test (section 3.3).

[8] Aspects of the Lagrangian statistics presented in section 3 are discussed in section 4. The asymptotic surfzone diffusivity  $\kappa$  dependence on surfzone conditions is explored (section 4.1). A previously proposed surfzone cross-shore diffusivity parameterization [e.g., Inman *et al.*, 1971] involving significant wave height and period does not reproduce the observed asymptotic cross-shore diffusivity. The asymptotic alongshore diffusivity variations correspond to variations in the surfzone mean alongshore current

maximum, consistent with a mixing-length model and shear dispersion [e.g., Taylor, 1953]. The observed non-Gaussian displacement pdfs at intermediate times are consistent with the observed cross-shore variation of Lagrangian statistics, reinforcing the “bulk” nature of the diffusivity estimates (section 4.2). Here unbiased diffusivity estimates are used, whereas previously [Spydell *et al.*, 2007] biased estimates were used. The sampling errors of the unbiased and biased diffusivity estimates are compared and depend on the number of trajectories, trajectory lengths, and the Lagrangian timescale (section 4.3). Results are summarized in section 5.

## 2. Observations

[9] Surfzone observations were collected near Huntington Beach CA as part of the Fall 2006 HB06 experiment. The cross-shore coordinate  $x$  increases negatively offshore ( $x = 0$  m is at the mean shoreline) and the alongshore coordinate  $y$  increases upcoast. The bathymetry was approximately alongshore uniform (Figure 1) and large rip channels were absent during the experiment. In particular, over the region that the drifters sample, the bathymetric nonuniformity statistic  $\chi^2 < 0.01$  was below the value found to induce circulation nonuniformities [Ruessink *et al.*, 2001]. Seven instrumented tripods were deployed on a cross-shore transect (at  $y = 0$  m) extending 160 m from near the shoreline to 4-m mean water depth (Figure 1, gray dots). Each tripod held a pressure sensor and a downward looking Acoustic Doppler Velocimeter (ADV) from which hourly wave (*e.g.*, significant wave height  $H_s$ ), and velocity statistics (mean and standard deviation) were calculated.

[10] Ten 50-cm tall, surfzone GPS-tracked drifters [Schmidt *et al.*, 2003], were deployed on five days (17 September and 2, 3, 14, and 15 October; Figure 1) with variable incident wave and mean current conditions (Table 1). Drifter data was collected for 5–6 hours beginning at 1000 local time. Drifters were released repeatedly (Figure 1, open white circles), within or near the surfzone, and allowed to drift freely for 15–30 minutes before being collected and re-released. Drifter tracks suggest advection by alongshore currents and the presence of low-frequency eddies (Figure 1). Drifters rarely advected offshore of the deepest instrumented tripod at  $x = -160$  m and drifters that came too close to shore and touched the bottom were collected and re-released farther offshore. Each drifter release and collection results in a separate drifter track. The number of tracks  $n_0$  varied between 59 and 70 with mean trajectory lengths  $T$  between 877 and 1376 s (Table 2, rows 1 and 2), for a daily total of 17–27 hours of drifter data.

[11] Each track consists of cross- and alongshore position time series  $\mathbf{X}(t) = (X(t), Y(t))$ , where  $t$  is time, sampled at 1 Hz. Absolute position errors are approximately  $\pm 2$  m. However, relative position errors, which induce velocity errors, are small and uncorrelated. Specifically, when drifters are at rest, the velocity variances (zero-lagged autocovariance) and diffusivities are three and four orders of magnitude, respectively, smaller than those observed for deployed drifters. Details of the data processing methods appears in the work of Spydell *et al.* [2007]. For each drifter track, time-located position and velocity data ( $X(t)$ ,  $Y(t)$ ,  $U(t)$ ,  $V(t)$ ) is calculated

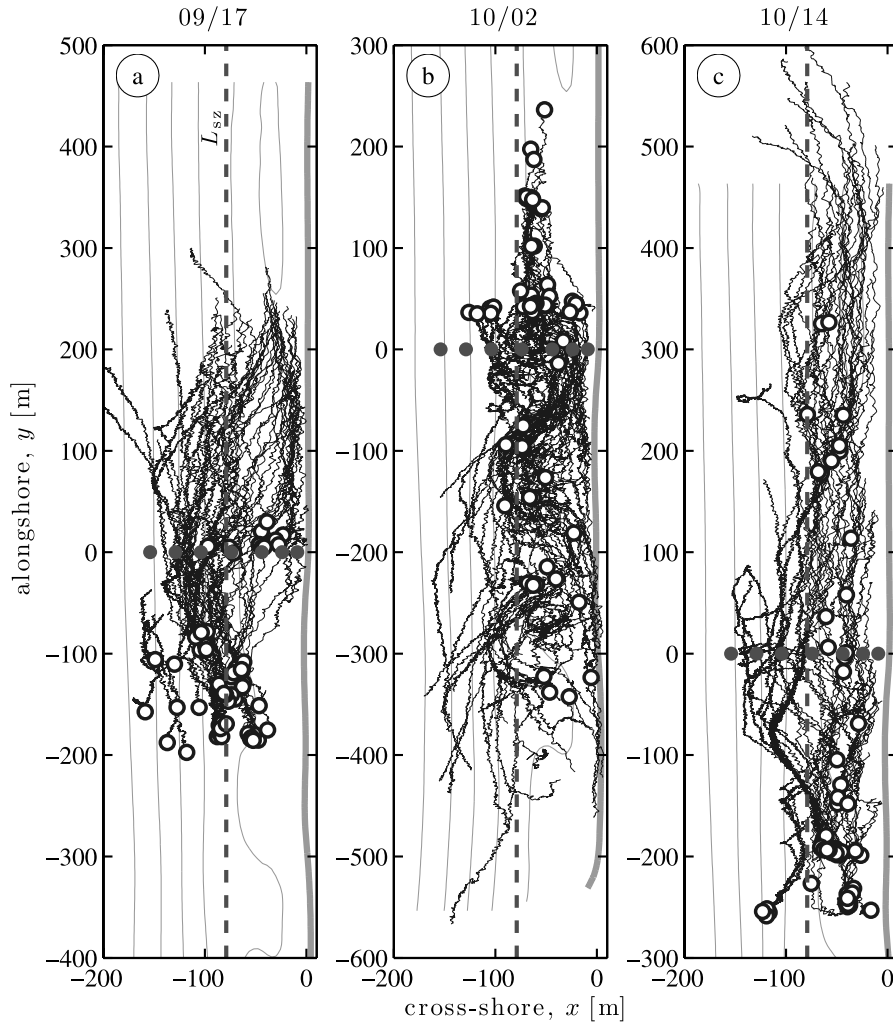


**Figure 1.** Drifter trajectories (black lines) on 3 days. White dots are drifter release locations, and the thick gray curve near  $x = 0$  m is the approximate waterline. Dashed gray line labeled  $L_{sz}$  indicates the outer edge of the surfzone. The instrumented cross-shore transect is indicated by dark gray dots at  $y = 0$  m. Bathymetry contours (thin gray), based on 43 approximately 25-m spaced (in the alongshore) cross-shore transects, are at 1-m intervals.

from the original positions via (for cross-shore position and velocity)

$$\frac{1}{2}[X(t+dt) + X(t)] \rightarrow \bar{X}(t)$$

$$\frac{X(t+dt) - X(t)}{dt} \rightarrow \bar{U}(t)$$
(1)

where  $dt = 1$  s, resulting in drifter positions and (2nd order accurate) velocities that are on the same time grid. Wave-averaged positions and velocities are obtained by smoothing  $X(t)$  and  $Y(t)$  with a Gaussian filter with a low-pass frequency cutoff of 0.033 Hz. Wave averaged quantities are denoted by tildes (e.g.,  $\bar{X}(t)$ ,  $\bar{U}(t)$ ) as are any statistics derived from them.

[12] The daily averaged incident wave heights, averaged over the drifter deployment on each day, spanned a relatively small range (between 0.65 and 0.83 m). The incident

mean wave frequency  $\bar{f}$ , directional spread  $\sigma_\theta$ , and surfzone width  $L_{sz}$  (Figure 1 and Table 1) were also approximately constant. However, mean wave direction  $\bar{\theta}$ , and the associated mean alongshore currents, varied significantly

**Table 1.** Eulerian Wave and Current Observations on the 5 Days of Drifter Releases<sup>a</sup>

Day	09/17	10/02	10/03	10/14	10/15
$H_s$ (m)	0.83	0.68	0.65	0.69	0.68
$\bar{f}$ (cps)	0.09	0.10	0.09	0.09	0.10
$\bar{\theta}$ (deg)	4.4	-4.0	-2.0	7.9	2.6
$\sigma_\theta$ (deg)	19	21	22	15	20
$\bar{v}_m$ (m s <sup>-1</sup> )	0.27	-0.13	-0.17	0.35	0.25
$L_{sz}$ (m)	99	74	79	79	79

<sup>a</sup>Statistics from the most offshore frame include the incident significant wave height  $H_s$ , mean frequency  $\bar{f}$ , mean direction  $\bar{\theta}$ , and directional spread  $\sigma_\theta$ . The maximum mean alongshore velocity  $\bar{v}_m$  excludes sensors 1 and 2, which often were close to the shoreline or out of the water. The surfzone width  $L_{sz}$  is obtained from energy fluxes.

**Table 2.** Lagrangian Drifter Statistics on Each Day<sup>a</sup>

Day	09/17	10/02	10/03	10/14	10/15
$n_0$	66	70	63	59	66
$T$ (s)	1110 ± 430	1376 ± 865	877 ± 722	1177 ± 823	1067 ± 701
$A_{xx}$ (m <sup>2</sup> s <sup>-2</sup> )	0.019 ± 0.001	0.032 ± 0.002	0.031 ± 0.002	0.020 ± 0.001	0.014 ± 0.001
$t_0$ (s)	312 ± 12	163 ± 10	172 ± 10	294 ± 9	1.82 × 10 <sup>6</sup>
$\tau_{xx}$ (s)	191 ± 13	125 ± 8	152 ± 11	339 ± 22	116 ± 8
$T_{xx}^{(L)}$ (s)	74 ± 3	29 ± 2	17 ± 2	-52 ± 18	116 ± 8
$\hat{\kappa}_{xx}^{\infty}$ (m <sup>2</sup> s <sup>-1</sup> )	1.38 ± 0.05	0.93 ± 0.04	0.53 ± 0.07	-1.03 ± 0.31	1.64 ± 0.02
Range $\hat{\kappa}_{xx}^{\infty}$ (m <sup>2</sup> s <sup>-1</sup> )	0.9–1.9	0.7–1.2	0.1–0.9	-1.4–(-0.7)	1.3–2.0
$A_{yy}$ (m <sup>2</sup> s <sup>-2</sup> )	0.029 ± 0.001	0.027 ± 0.002	0.034 ± 0.002	0.048 ± 0.001	0.029 ± 0.001
$\tau_{yy}$ (s)	342 ± 11	190 ± 13	118 ± 7	390 ± 9	419 ± 33
$\hat{\kappa}_{yy}^{\infty}$ (m <sup>2</sup> s <sup>-1</sup> )	10.0 ± 0.12	5.15 ± 0.09	3.94 ± 0.05	18.6 ± 0.19	12.0 ± 0.43
Range $\hat{\kappa}_{yy}^{\infty}$ (m <sup>2</sup> s <sup>-1</sup> )	7.5–12.7	4.2–6.1	3.0–5.0	14.0–23.7	8.9–15.7

<sup>a</sup>The first two rows are total number of drifter trajectories  $n_0$  and the mean trajectory length  $T$  ( $\pm 1$  std). The coefficients of the fitted LVAf (9) and (7) and asymptotic quantities derived therefrom (e.g.,  $\hat{\kappa}^{\infty}$ ) follow. Fit errors (Appendix C) are indicated as  $\pm$ 's. On 10/15 the  $t_0$  error is not calculated and the asymptotic errors are calculated assuming  $t_0 \rightarrow \infty$ . The range of the asymptotic  $\hat{\kappa}_{xx}^{\infty}$  (and  $\hat{\kappa}_{yy}^{\infty}$ ) indicates likely values (the approximately 68% range) of  $\hat{\kappa}_{xx}^{\infty}$  that would result with repeated experiments, i. e., the range is the asymptotic diffusivity sampling error (Appendix D).

over the five days (Table 1). Consistent with the sign of the bulk incident wave angles, the maximum alongshore current  $\bar{v}_m$  was positive on 09/17, 10/14, and 10/15 due to the predominant south swell, and negative on 10/02, and 10/03 as a result of westerly wind swell. Although the alongshore current was generally weak, the  $\bar{v}_m$  magnitude varied between 0.13 and 0.35 m s<sup>-1</sup>, almost a factor of three. Wave conditions on each day did not change significantly over the 5–6 hours of drifter releases. The maximum variation in incident  $H_s$  was 0.05 m.

[13] Eulerian mean and standard deviation (std) velocities estimated from cross-shore binned (12–19 m bin size) drifter velocities are usually similar to values from the instrumented tripods (Figure 2). For example, the mean alongshore current  $\bar{v}$  (Figure 2a) and cross-shore velocity standard deviation  $\text{std}(u)$  (Figure 2b) compare well. On all days, offshore of the surfzone  $\text{std}(u) \approx 0.2$  m s<sup>-1</sup> and increases due to wave shoaling shoreward to a maximum at  $x \approx -75$  m followed by a shoreward decrease owing to wave breaking. Alongshore velocity standard deviation  $\text{std}(v)$  also are similar on all days with  $\text{std}(v) \approx 0.1$  m s<sup>-1</sup> offshore of wave breaking and increasing shoreward (Figure 2c). However, for unknown reasons the drifter derived  $\text{std}(v)$  is larger than the ADV observed within the inner surfzone ( $x > -75$  m). Drifter sampling was usually most concentrated (approximately 3 drifter hours per day) in the midouter surfzone ( $x \approx -90$  m), and was more evenly distributed on 10/14 (Figure 2d). The difference between observed between drifter- and ADV observed  $\bar{v}$  is increased close to the shoreline (Figure 2a) at least in part by the relative paucity of near shoreline drifter sampling (Figure 2d) and the increased alongshore velocity variability within the surfzone (Figure 2c).

### 3. Single-Particle Lagrangian Statistics

[14] The mean Lagrangian displacement is defined as

$$\bar{X}(t) = \langle X(t) - X(0) \rangle \quad (2)$$

where the average “ $\langle \cdot \rangle$ ” is over all drifter tracks and all possible  $t = 0$  along a drifter track (Appendix A). In

statistically stationary flows, the release time  $t = 0$  is arbitrary along the drifter track, and averaging over all  $t = 0$  (i.e., all possible  $t$  lags) is possible. Thus single-particle statistics could be calculated from one drifter track. Anomalous displacement ( $r_x, r_y$ ) are defined as

$$r_x(t) = X(t) - X(0) - \bar{X}(t), \quad (3)$$

and anomalous velocities ( $u(t), v(t)$ ) are defined similarly.

[15] Tracer evolution, in both homogeneous and inhomogeneous flows, can be modeled by a Fickian diffusion equation with the diffusivity obtained from single-particle (or absolute) Lagrangian statistics [Davis, 1987]. Three key related Lagrangian statistics are the Lagrangian velocity autocovariance function (LVAf)

$$C_{xx}(t) = \langle u(t)u(0) \rangle, \quad (4)$$

the absolute diffusivity, or ensemble tracer patch spreading rate,

$$\kappa_{xx}(t) = \int_0^t C_{xx}(t') dt', \quad (5)$$

and the absolute dispersion  $D^2$ , or ensemble tracer patch size squared,

$$D_{xx}^2(t) = 2 \int_0^t \kappa_{xx}(t') dt'. \quad (6)$$

The dispersion  $[D^2(t)]^{1/2}$  can be interpreted as the half-width of the ensemble-averaged tracer patch at time  $t$  originally released as a delta function. Subscripts denote tensor components, with the  $yy$  component calculated analogously (with  $x \rightarrow y$  and  $u \rightarrow v$  in equations (4), (5), and (6)). Only the diagonal tensor components are analyzed here. The LVAf  $C(t)$  is estimated directly from anomalous drifter velocities with the diffusivity  $\kappa(t)$  and dispersion  $[D^2(t)]^{1/2}$  derived from  $C(t)$  [e.g., Davis, 1987; Spydell et al., 2007].

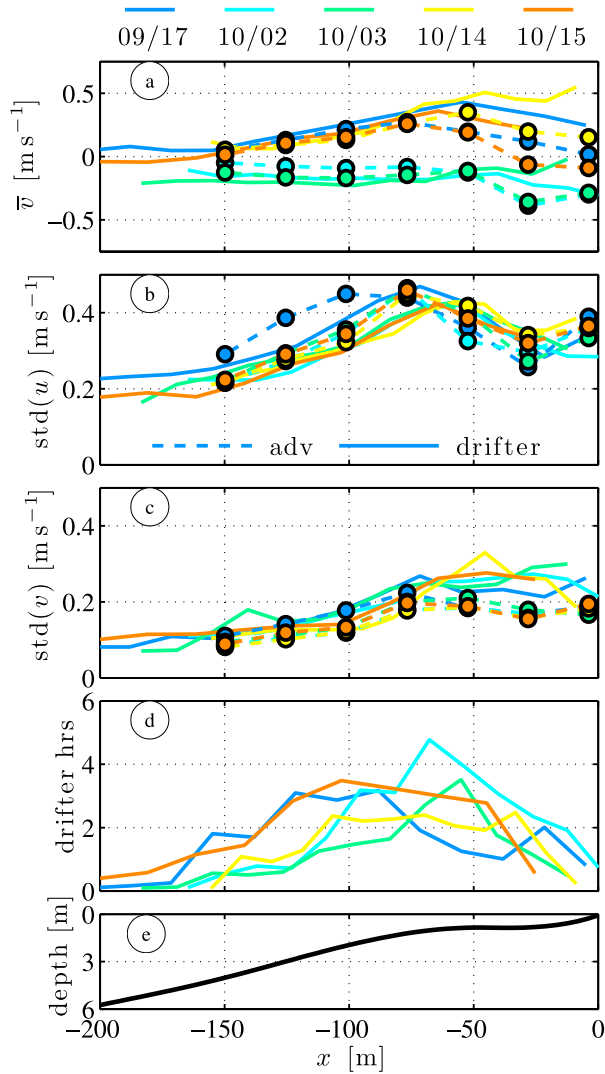


**Figure 2.** Binned drifter (solid lines) and fixed instrument (dashed lines with dots) Eulerian velocity statistics versus the cross-shore coordinate  $x$  on each day (colors): (a) mean alongshore currents ( $\bar{v}$ ), (b) standard deviation of cross-shore velocities ( $\text{std}(u)$ ), (c) standard deviation of alongshore velocities ( $\text{std}(v)$ ), (d) drifter hours in each bin, and (e) mean depth. Cross-shore bin width varies between 12 and 19 m, depending on the day.

### 3.1. Observed Lagrangian Velocity Autocovariance, Diffusivity, and Dispersion

[16] Full (unaveraged) and wave-averaged drifter velocities are used in equation (4) to calculate the Lagrangian velocity autocovariances  $C(t)$  and  $\hat{C}(t)$ , respectively (Figure 3). Oscillations in  $C_{xx}(t)$  from cross-shore orbital wave velocities are evident for  $t < 30$  s and decay after many incident wave periods (Figure 3a), i.e.,  $C_{xx}(t) \approx \hat{C}_{xx}(t)$  for  $t > 100$  s. For  $t > 150$  s, both  $C_{xx}$  and  $\hat{C}_{xx}$  are negative, reaching a minimum near  $t \approx 300$  s (Figure 3a). For about  $t \geq 1000$  s, large errors in both cross- and alongshore  $C(t)$  estimates result from relatively few observations and cause large  $C(t)$  oscillations, limiting useful diffusivity and dispersion estimates to  $t < 1000$  s. Sampling errors are discussed in section 4.3.2.

[17] Large oscillations at short times are not present in  $C_{yy}$  (Figure 3b) as alongshore orbital wave velocity motions are weak. The wave-averaged  $\hat{C}_{yy}$  closely follows  $C_{yy}$  for  $t > 10$  s (Figure 3, compare thin- and thick-dashed curves). After  $t > 20$  s, both  $C_{yy}$  and  $\hat{C}_{yy}$  decrease exponentially. Unlike  $\hat{C}_{xx}$ ,  $\hat{C}_{yy}$  is (within 68% confidence limits) positive for  $t < 1000$  s.

[18] Bulk surfzone absolute diffusivities  $\kappa$  (Figure 4), calculated using the non-wave-averaged LVA  $C(t)$  in equation (5), are representative of drifters deployed in, and remaining in, the surfzone for  $t < 1000$  s (Figure 1). With longer deployments, a fraction of drifters presumably would eventually leave the surfzone and be subject to inner-shelf processes resulting in different Lagrangian statistics (i.e., diffusivities).

[19] Generally (except on 10/15), the cross-shore diffusivity  $\kappa_{xx}(t)$  reaches a maximum around  $1.5 \text{ m}^2 \text{ s}^{-1}$  between  $t = 160\text{--}300$  s, before slowly decreasing. On all days, the long-time cross-shore diffusivity,  $\kappa_{xx}(t)$  at  $t = 1000$  s, varies between 0.5 and  $2 \text{ m}^2 \text{ s}^{-1}$ . However, the  $\kappa_{xx}$  error bars (Appendix B) often overlap for  $t > 600$  s (shaded regions in Figure 4), so long-time  $\kappa_{xx}$  values are only marginally statistically different. On all days, the alongshore diffusivity  $\kappa_{yy}(t)$  monotonically increases in time, with the most rapid increases at short time (Figure 4b). On 10/02 and 10/03,  $\kappa_{yy}$  are approximately constant for  $t > 500$  s. At longer times ( $t > 200$  s),  $\kappa_{yy} > \kappa_{xx}$  (Figure 4).

[20] Similar to previous observations [Spydell et al., 2007], at short times the patch-size cross shore  $[D_{xx}^2]^{1/2}$  is larger than alongshore  $[D_{yy}^2]^{1/2}$  (compare dashed-colored with solid-colored curves for  $t < 20$  s in Figure 5b). At longer times, in accordance with the larger alongshore diffusivities, patches become alongshore elongated with  $[D_{yy}^2]^{1/2} > [D_{xx}^2]^{1/2}$  (Figure 5, compare solid with dashed curves).

[21] On all days, the cross-shore patch half-widths  $[D_{xx}^2]^{1/2}$  at longer times ( $t > 500$  s) are similar, with  $[D_{xx}^2]^{1/2} \approx 50$  m (Figure 5a, dashed lines). As typical surfzone widths are  $L_{sz} \approx 100$  m, it takes approximately 500 s for the ensemble-averaged patch, released in the center of the surfzone, to spread across the surfzone. In contrast, the alongshore patch half-width  $[D_{yy}^2]^{1/2}$  varies considerably at long times, between approximately 80–150 m at  $t = 1000$  s (Figure 5a, solid lines).

### 3.2. Analytic Forms: Asymptotic Diffusivities and Lagrangian Timescales

[22] Functional forms for the LVA  $\hat{C}$ , diffusivity  $\hat{\kappa}$ , and dispersion  $\hat{D}^2$  facilitate calculation and interpretation of single-particle statistics (e.g., asymptotic diffusivities), and simplify estimation of sampling errors. The autocovariance for a first order autoregressive process [e.g., LaCasce, 2008] has the form  $\sim \exp(-t)$  as does the Lagrangian velocity autocovariance for modeled turbulent flow [e.g., Yeung and Pope, 1989; Mordant et al., 2003]. Therefore the following functional form for the alongshore LVA is used,

$$\hat{C}_{yy}(t) = A_{yy} \exp(-|t|/\tau_{yy}) \quad (7)$$

where  $A_{yy}$  is the zero-lag Lagrangian velocity autocovariance (i.e., the variance) and  $\tau_{yy}$  is the alongshore

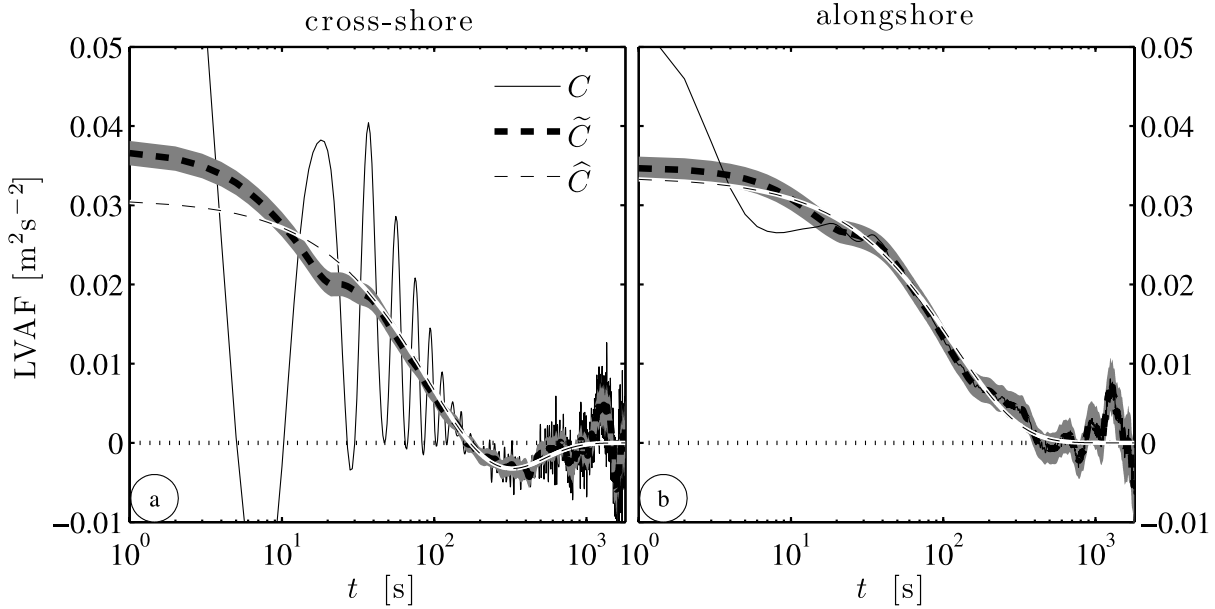


**Figure 3.** Lagrangian velocity autocovariance functions (LVAFs) on 10/03 versus time: (a) cross-shore  $C_{xx}$  and (b) alongshore  $C_{yy}$ . Thin, thick-dashed, and thin-dashed curves are LVAFs derived from velocities with waves  $C$ , wave-averaged velocities  $\tilde{C}$ , and the best fit analytic function  $\hat{C}$ , respectively. Error bars (Appendix B) or 68% confidence on  $\hat{C}$  are indicated by gray shading.

Lagrangian timescale. Using this  $\hat{C}$ , the analytic alongshore diffusivity is

$$\hat{\kappa}_{yy}(t) = \int_0^t \hat{C}_{yy}(t') dt' = A_{yy} \tau_{yy} [1 - \exp(-|t|/\tau_{yy})]. \quad (8)$$

For  $t > 200$  s, the observed negative  $C_{xx}$  (Figure 3a) is captured with a modified functional form for  $\hat{C}_{xx}$ ,

$$\hat{C}_{xx}(t) = A_{xx} (1 - |t|/t_0) \exp(-|t|/\tau_{xx}). \quad (9)$$

The factor  $(1 - |t|/t_0)$  in equation (9) makes  $\hat{C}_{xx}(t) < 0$  for  $t > t_0$  similar to the observed  $C_{xx}$  (Figure 3). The analytic cross-shore diffusivity is then

$$\begin{aligned} \kappa_{xx}(t) &= \int_0^t \hat{C}_{xx}(t') dt' \\ &= A_{xx} \tau_{xx} \left( \left[ 1 - \frac{\tau_{xx}}{t_0} \right] [1 - \exp(-|t|/\tau_{xx})] + \frac{|t|}{t_0} \exp(-|t|/\tau_{xx}) \right) \end{aligned} \quad (10)$$

resulting in a  $\hat{\kappa}_{xx}$  maximum similar to that observed (Figure 4).

[23] The parameters  $\beta = [A_{xx}, t_0, \tau_{xx}]$  ( $[A_{yy}, \tau_{yy}]$  for  $\kappa_{yy}$ ) are found by minimizing the squared misfit between observed and fitted  $\kappa(t)$ , i.e.,

$$G(\beta) = \int_0^{T_m} [\kappa_{xx}(t) - \hat{\kappa}_{xx}(\beta, t)]^2 dt \quad (11)$$

is minimized for the cross-shore diffusivity. The integral upper limit  $T_m = 1000$  s avoids the large and rapidly

growing sampling errors at longer times. Fit parameters are given in Table 2.

[24] The observed  $\kappa$  and fitted  $\hat{\kappa}$  are similar (with fit skill  $> 0.98$ ) in both directions on all 5 days (Figure 4, compare colored with dashed black curves). Similarly, fit  $\hat{C}_{yy}$  is similar to the observed  $C_{yy}$  for  $t > 10$  s (Figure 3b) but in the cross shore it is the fit  $\hat{C}_{xx}$  and the wave-averaged velocity derived  $\tilde{C}_{xx}$  that are similar (Figure 3a). Thus consistent with previous field [Spydell *et al.*, 2007] and numerical [Spydell and Feddersen, 2009] surfzone drifter studies, the observed diffusivity  $\kappa$  is due to wave-averaged processes. Surface gravity wave orbital velocities are merely noise in the context of surfzone drifter dispersion.

[25] As  $t \gg \tau_{xx}$ , the fit  $\hat{\kappa}(t)$  becomes the fit asymptotic cross-shore and alongshore diffusivities  $\hat{\kappa}^\infty$ , i.e., in the cross shore

$$\hat{\kappa}_{xx}^\infty = A_{xx} \tau_{xx} (1 - \tau_{xx}/t_0) \quad (12)$$

and in the alongshore

$$\hat{\kappa}_{yy}^\infty = A_{yy} \tau_{yy},$$

which is the classic asymptotic diffusivity expression [Taylor, 1921]. This extrapolation of  $\hat{\kappa}(t)$  to long times assumes that the analytic LVAF equation (9) is valid for  $t > 1000$  s.

[26] If  $\tau_{xx} < t_0$ , the  $\hat{\kappa}_{xx}^\infty$  are positive indicating a diffusive processes. On all days except 10/14,  $\hat{\kappa}_{xx}^\infty$  is positive and is between 0.7 and 1.7  $\text{m}^2 \text{s}^{-1}$ . On 10/14,  $t_0 > \tau_{xx}$  and  $\hat{\kappa}_{xx}^\infty$  is negative (Table 2) due to drifter convergence close to shore at  $y \geq 200$  m for long times (Figure 1c). Throughout the day, drifters converged near the shore, with only 3 of 32 tracks having cross-shore positions  $< -100$  m when

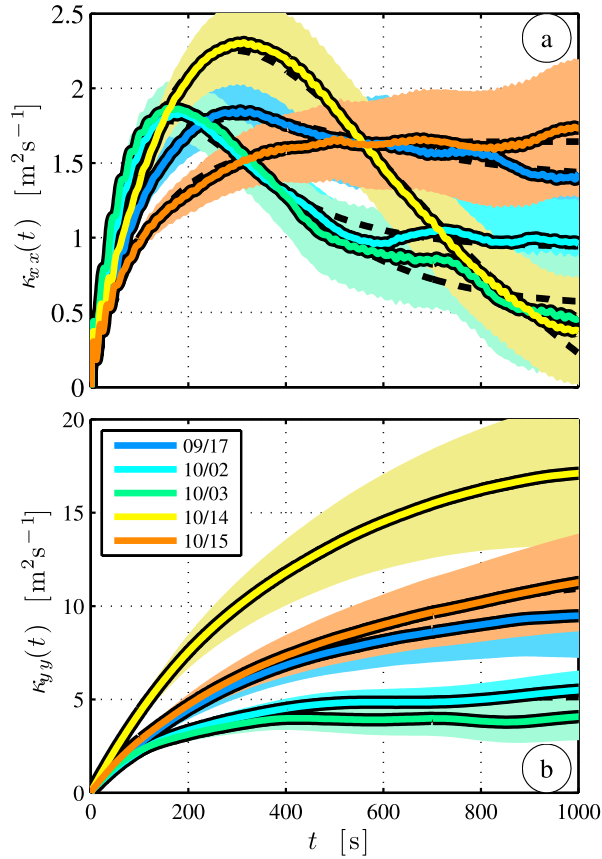


**Figure 4.** Single-particle diffusivity  $\kappa$  versus time for each day (indicated by color): (a) cross-shore  $\kappa_{xx}(t)$  and (b) alongshore  $\kappa_{yy}(t)$ . Diffusivities are derived directly from the data with waves (colored curves) with sampling error (68% confidence limit, light-colored shading) and from the best fit analytic  $\hat{\kappa}(t)$  (dashed black line).

alongshore positions are  $>200$  m. Hence this negative  $\kappa_{xx}$  is possibly due to an underlying convergent mean flow (potentially bathymetrically controlled) which is not a diffusive process.

[27] The asymptotic cross-shore diffusivity  $\hat{\kappa}_{xx}^{\infty}$  fit is usually good as fit errors (representing goodness of fit, Appendix C) range between 1.2% and 30% (number after the  $\pm$  in Table 2). Only 10/14 has a fit error larger than 14%. However, the  $\hat{\kappa}_{xx}^{\infty}$  sampling errors (Appendix D), representing the RMS  $\kappa_{xx\infty}$  range that would be obtained in a different realizations of an identical experiment, are larger 20–80% (see “range  $\hat{\kappa}_{xx}^{\infty}$ ” in Table 2). On the five days, the alongshore asymptotic diffusivity  $\hat{\kappa}_{yy}^{\infty}$  spans a much broader range ( $4 < \hat{\kappa}_{yy}^{\infty} < 19$   $\text{m}^2 \text{s}^{-1}$ ) than  $\hat{\kappa}_{xx}^{\infty}$  (Table 2) with  $\hat{\kappa}_{yy}^{\infty}$  fit and sampling errors smaller than those for  $\hat{\kappa}_{xx}^{\infty}$  (1–3.6% and 18–31% respectively, Table 2).

[28] Theoretically, at short times,  $t \ll \tau$ , Lagrangian velocities are correlated and dispersion is ballistic ( $D^2 \sim t^2$ ) whereas for long times, Lagrangian velocities are uncorrelated and dispersion is Brownian ( $D^2 \sim t$ ). The Lagrangian timescale, defined as  $T^{(L)} = \hat{\kappa}^{\infty}/\hat{C}(t=0)$ , characterizes the transition between ballistic ( $t \ll T^{(L)}$ ) and Brownian ( $t \gg T^{(L)}$ ) dispersion regimes. The alongshore Lagrangian time-

scale  $T_{yy}^{(L)} = \tau_{yy}$ , ranges from 118 to 419 s (Table 2) and the cross-shore Lagrangian timescale,  $T_{xx}^{(L)} = \tau_{xx}(1 - \tau_{xx}/t_0)$  is  $< \tau_{xx}$  and varies between 17 and 116 s, except on 10/14 where it is negative (Table 2).

[29] From the analytic LVAE equations (7) and (9), the ballistic (short time) regime ( $t \ll T^{(L)}$ ) is,

$$[\hat{D}_{xx}^2]^{1/2} \sim A_{xx}^{1/2} t \quad (13)$$

with  $xx$  replaced by  $yy$  for the alongshore. For short times ( $t < 20$  s), the ballistic scaling (13) underpredicts both the cross- and alongshore dispersion (Figure 5), because analytic LVAEs do not include surface gravity wave contributions, only important at these times, particularly in the cross shore (see Figure 3a). Thus the surface gravity wave motions that result in large differences at short times between  $C_{xx}(t)$  and  $\hat{C}_{xx}(t)$  (Figure 3), only cause significant differences in the observed (with waves) dispersion  $[D_{xx}^2]^{1/2}$  and fitted dispersion  $[\hat{D}_{xx}^2]^{1/2}$  for  $t \lesssim 20$  s (Figure 5b). However, at these times the patch sizes are small ( $[D_{xx}^2]^{1/2}$  and  $[D_{yy}^2]^{1/2}$  are  $< 3$  m). The similarity between the analytic LVAE fit  $\hat{\kappa}$  and  $\kappa$  and therefore between  $\hat{D}$  and  $[D^2]^{1/2}$  for  $t > 20$  s demonstrate that surfzone drifter dispersion is due to motions with frequencies below surface gravity wave frequencies. Unlike  $[D_{xx}^2]^{1/2}$  which never closely follows a ballistic scaling (Figure 5b, compare dashed colored and dashed black curves), the alongshore dispersion  $[D_{yy}^2]^{1/2}$  is ballistic for  $30 \text{ s} < t < \tau_{yy}$  (Figure 5b, black solid curve).

[30] From the analytic LVAE, the Brownian regime ( $t \gg T^{(L)}$ ) is

$$[\hat{D}_{xx}^2]^{1/2} \sim [2A_{xx}\tau_{xx}(1 - \tau_{xx}/t_0)t]^{1/2} \quad (14)$$

$$[\hat{D}_{yy}^2]^{1/2} \sim [2A_{yy}\tau_{yy}t]^{1/2}. \quad (15)$$

Because  $T_{xx}^{(L)} < T_{yy}^{(L)}$ , the observed cross-shore dispersion  $[D_{xx}^2]^{1/2}$  is within 90% of Brownian  $[\hat{D}_{xx}^2]^{1/2}$  for  $t \gtrsim 200$  s whereas the observed  $[D_{yy}^2]^{1/2}$  does not reach Brownian scaling at  $t = 1000$  s (Figure 5a, thin dashed and thin solid curves are 09/17 Brownian scalings). In particular, according to the fit LVAE parameters,  $[D_{yy}^2]^{1/2}$  would be within 90% of the Brownian scaling for  $t \geq 5.25 \tau_{yy}$  or for times  $>2000$  s. Thus the HB06 drifter trajectories are too short to observe alongshore Brownian motion.

### 3.3. Drifter Displacements

[31] From the probability distribution function (pdf) of displacements, aspects of the mixing processes can be inferred. In particular, Gaussian pdfs are expected for homogeneous mixing while non-Gaussian pdfs result from inhomogeneous mixing or coherent structures present in the flow [e.g., Pasquero *et al.*, 2001]. The pdf of cross-shore displacements  $P(r_x)$ , and alongshore displacements  $P(r_y)$ , is calculated on all days for all  $t$  displacements. The pdfs are normalized to zero mean and unit standard deviation ( $t = 1, 30, \text{ and } 500$  s for 10/02 are shown in Figure 6).

[32] Displacement pdfs generally fall into three categories: (1) Gaussian-like, (2) peakier than Gaussian, and (3) “noisy”.

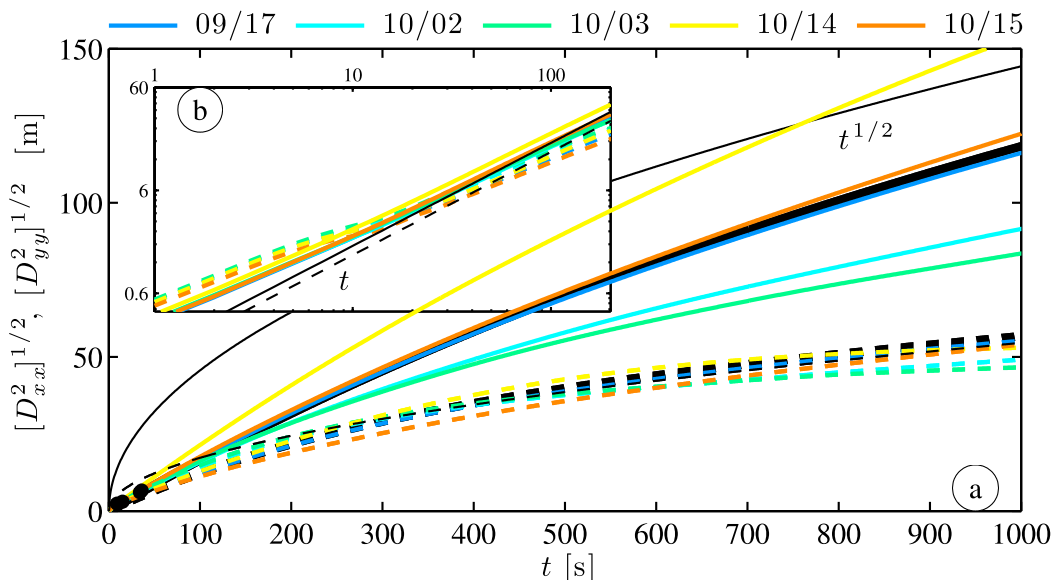


**Figure 5.** The cross-shore  $[D_{xx}^2]^{1/2}$  (dashed) and alongshore  $[D_{yy}^2]^{1/2}$  (solid) dispersion versus time (color corresponds to day). Figure 5a has a linear-linear axis. The thick-dashed and thick-solid curves are the fitted 09/17 cross- and alongshore dispersion  $[\hat{D}^2]^{1/2}$ , respectively. The 09/17 Brownian (long time,  $t^{1/2}$  growth) regime for the cross shore and alongshore (equations (14) and (15)) is given by the thin-dashed and thin-solid black curves, respectively. The cross-shore Brownian follows the  $[D_{xx}^2]^{1/2}$  (thick- and thin-dashed curves overlap). The alongshore Brownian curve, labeled with a  $t^{1/2}$ , does not follow  $[\hat{D}_{yy}^2]^{1/2}$  (thin- and thick-solid curves do not overlap). Figure 5b has a log-log axis for  $1 < t < 200$  s. The 09/17 cross- and alongshore (short-time) ballistic regimes (equation (13)) are indicated as thin-dashed and thin-solid curves, respectively.

Gaussian-like cross- and alongshore displacement pdfs are found for small  $t$  ( $t = 1$  s, Figures 6a and 6b, blue lines), and peakier than Gaussian pdfs are often found for intermediate  $t$  (e.g.,  $t = 30$  s, Figure 6a, green line). As  $t$  increases, there are less observations and pdfs become noisy (e.g.,  $t = 500$  s,

Figures 6a and 6b, red lines). Given finite observations, the degree to which these pdfs truly are or are not Gaussian is unclear. Previously, normalized displacement pdfs were inferred to be largely Gaussian in the surfzone, however, data plotted with a logarithmic ordinate obscured departures

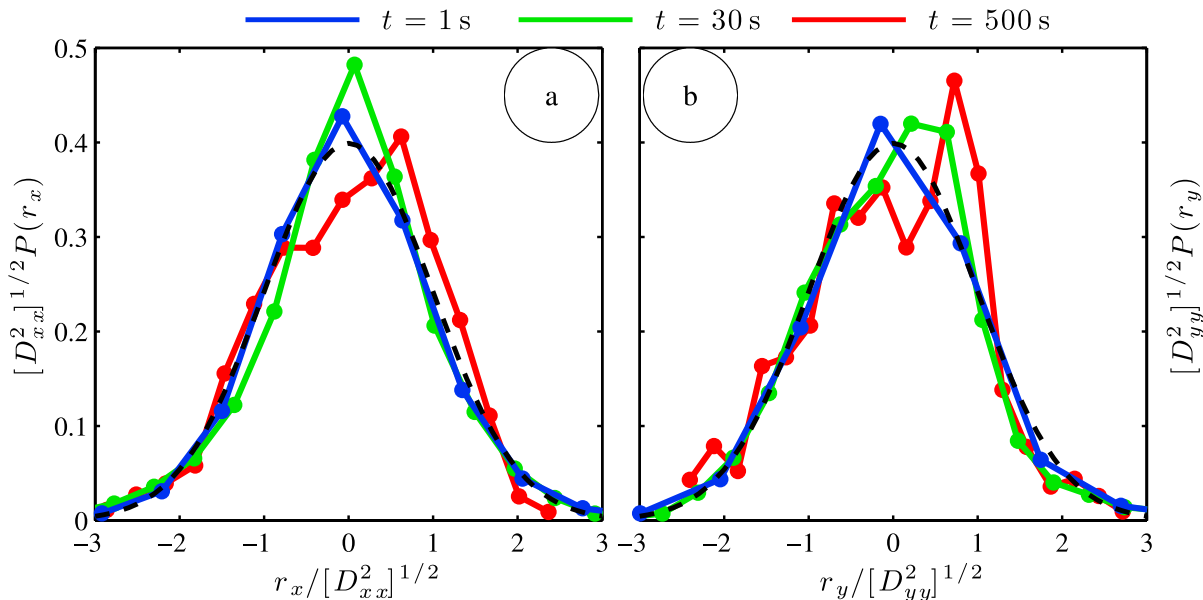


**Figure 6.** The observed normalized probability density function versus normalized displacements at the times  $t = 1$ , 30, and 500 s (colors) on 10/02: (a) cross-shore displacements and (b) alongshore displacements. The dashed line is a Gaussian.

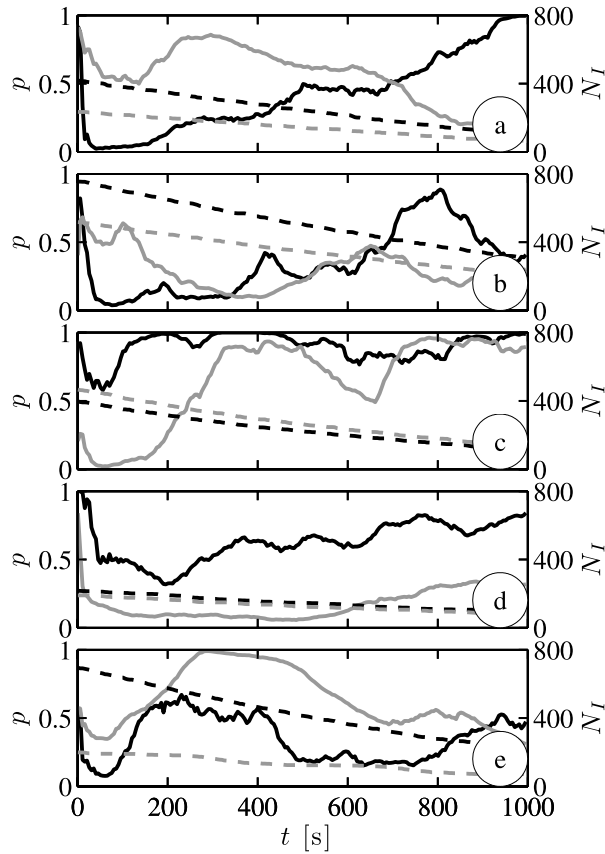


**Figure 7.** Komolgorov-Smirnov (K-S) test  $p$  values (left axis, solid curves:  $p_x$ , black;  $p_y$ , gray) and the number of independent displacements  $N_I$  (right axis, dashed curves:  $x$ , black;  $y$ , gray) versus time  $t$  for (a) 09/17, (b) 10/02, (c) 10/03, (d) 10/14, and (e) 10/15.

from Gaussian and no quantitative tests were applied [Spydell and Feddersen, 2009].

[33] The likelihood that displacement pdfs are Gaussian is determined from a Kolmogorov-Smirnov (K-S) test, which tests the null hypothesis: “the data is standard normal at the  $\alpha$  significance level”. The test statistic  $d$  is the maximum absolute difference between the observed normalized-displacement cumulative distribution function (cdf) and a standard normal cdf. The K-S test inputs are the test statistic  $d$  and the number of independent observations  $N_I$  and the K-S test returns the probability  $p$  (P value) of obtaining a value of  $d$  or larger by chance given  $N_I$ . The null hypothesis is rejected at the  $\alpha$  significance level if  $p < \alpha$ . Thus displacement pdfs are more likely Gaussian for larger  $p$ . However, even at lower values of  $p$ , there is still a reasonable (e.g., for  $p = 0.5$  a 50%) likelihood that the observed pdf is actually Gaussian. Thus the pdf is not Gaussian with confidence unless  $p$  is very small ( $< 0.05$ ). Furthermore, as  $p \sim 2\exp(-2d^2N_I)$  for large  $N_I$  ( $> O(10^2)$ ), larger samples are less likely to be Gaussian for the same  $d$ . This test is applied on all days for  $t < 1000$  s in both directions giving cross- and alongshore P values  $p_x$  and  $p_y$ , respectively. However, the number of independent displacements  $N_I$  at each  $t$  first must be determined.

[34] The total number of independent displacements  $N_I(t)$  (Figure 7, dashed lines, right axis) is the sum over the number of independent displacements in each track

$$N_I(t) = \sum_{j=1}^{n(t)} \text{ceil}[(T_j - t)/\tau], \quad (16)$$

where  $n(t)$  is the number of tracks longer than  $t$ ,  $T_j$  is the length of the  $j$ th track,  $\tau$  is either  $\tau_{xx}$  or  $\tau_{yy}$  depending on the direction, and ceil rounds up to the nearest integer. Except on 10/03 and 10/14 where  $\tau_{xx} > \tau_{yy}$ , the cross-shore  $N_I$  is larger than alongshore  $N_I$  for all  $t$  (Figure 7, right axis) leading to noisier alongshore pdfs than cross-shore pdfs (Figures 6a and 6b, compare red lines). The estimate of  $N_I$  neglects spatial correlation between drifters, resulting in  $N_I$  overestimates and  $p$  underestimates.

[35] The likelihood as measured by  $p$  that the displacements are Gaussian varies considerably in day, time, and direction (Figure 7, left axis). On most days, except 10/15, for short times ( $t < 15$  s),  $p_x$  is near one (Figure 7, black solid curves) indicating that displacements are probably Gaussian, consistent with the similarity between the observed pdf and the Gaussian ( $t = 1$  s, Figure 6a, blue curve). At intermediate times,  $p_x$  decreases and reaches a minimum near  $t = 75$  s. On 09/17, 10/02, and 10/14,  $p_x$  generally increases for  $200 < t < 1000$  s, indicating that the displacement pdfs are more likely Gaussian at longer times. On 10/03, cross-shore displacement pdfs are probably Gaussian for all  $t > 100$  s. The alongshore  $p_y$  is more variable than  $p_x$  in time and across days (Figure 7, compare gray to dark solid curves). Alongshore displacements are most likely to be Gaussian only on 10/03 for  $t > 400$  s, on 09/17 for  $t$  close to zero and for  $200 < t < 400$  s, and on 10/15 for  $200 < t < 500$  s.

[36] At intermediate times  $20 < t < 200$  s, the consistently low  $p_x$  values from the K-S test indicate that cross-shore displacement pdfs are probably not Gaussian, but are more likely Gaussian at very short and longer times. Thus the  $t = 30$  s peakier than Gaussian pdf (Figure 6a, green line) appears real and is not an artifact of undersampling. A potential mechanism to explain this is discussed in section 4.2.

## 4. Discussion

### 4.1. Parameterizing the Asymptotic Diffusivity

[37] The effect of varying surfzone conditions on fit asymptotic diffusivities  $\hat{\kappa}_{xx}^\infty$  and  $\hat{\kappa}_{yy}^\infty$  is now examined. Inman *et al.* [1971] link  $\kappa_{xx}$  to the incident significant wave height  $H_s$  and mean frequency  $\bar{f}$  (Table 1) via

$$\kappa_{xx} \simeq \alpha H_s^2 \bar{f} \quad (17)$$

without any explicit diffusivity time dependence. Recently, a similar relationship was obtained with a simple model of surfzone cross-shore tracer diffusion by bores [Feddersen, 2007; Henderson, 2007] where  $\kappa_{xx}$  in equation (17) is the wave-averaged cross-shore tracer diffusivity due to bores. For HB06 conditions, the scaling in Feddersen [2007] predicts  $\alpha \approx 1.25$ . However, note that by design surfzone drifters duck under and are not entrained in or dispersed by bores [Schmidt *et al.*, 2003].

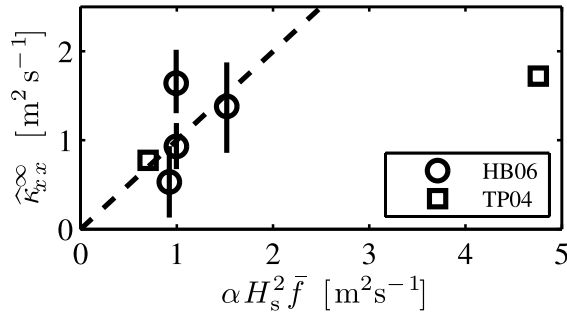


**Figure 8.** The HB06 asymptotic cross-shore diffusivity  $\hat{\kappa}_{xx}^\infty$  versus  $\alpha H_s^2 \bar{f}$  (circles) with best fit  $\alpha = 20.9 \pm 5$  and fit skill of 0.2. Wave height  $H_s$  and mean frequency  $\bar{f}$  are estimated from the most offshore frame. Vertical lines indicated  $\hat{\kappa}_{xx}^\infty$  error bars (Appendix D). The negative  $\hat{\kappa}_{xx}^\infty$  on 10/14 is not shown and is excluded from the linear best fit (dashed line). Also shown (but not included in the fit) are TP04 [Spydell et al., 2007] data points. Due to data limitations, TP04 error bars could not be calculated.

[38] Using the incident  $H_s$  and  $\bar{f}$  (Table 1) and the 4 days with positive  $\hat{\kappa}_{xx}^\infty$ , the fit to equation (17), constrained to go through the origin, results in  $\alpha = 20$  with low skill (0.20) (Figure 8). Fitting to the maximum  $\hat{\kappa}_{xx}$  instead of  $\hat{\kappa}_{xx}^\infty$  results in a similarly poor skill. However, the parameterization (17) cannot be verified or dismissed by the present observations for the following reasons: there are only four HB06 data points, the range of  $\alpha H_s^2 \bar{f}$  is small ( $1-1.5 \text{ m}^{-2} \text{ s}^{-1}$ ), and the  $\hat{\kappa}_{xx}^\infty$  sampling error (Figure 8, vertical bars) overlap such that the  $\hat{\kappa}_{xx}^\infty$  are not distinctly different. The present observations do not conclusively test the parameterization (17).

[39] Two days of surfzone Lagrangian drifter data [Spydell et al., 2007] were also collected in 2004 at Torrey Pines Beach CA (TP04). The data were reprocessed with unbiased autocovariances and best fit to the analytic LVAf for consistency with the HB06 data. The TP04 day one with small waves ( $H_s = 0.5 \text{ m}$ ) is consistent with the HB06 data and

agrees reasonably with equation (17) and  $\alpha \approx 20$  whereas TP04 day two with large  $H_s = 1.35 \text{ m}$  does not (see Figure 8, squares).

[40] Although the fit skill to equation (17) is poor, the best fit  $\alpha \approx 20$  is significantly larger than expected for bore-induced dispersion ( $\alpha \approx 1.25$ ). Thus  $\hat{\kappa}_{xx}^\infty$  is larger than that expected for tracer mixing by idealized periodic bores. Moreover, the bore-induced  $\kappa_{xx}$  timescale is expected to be a few wave periods whereas here  $\tau_{xx} \approx 150 \text{ s}$ , consistent with long-time drifter dispersion caused by low-frequency vortical motions [Spydell and Feddersen, 2009]. Thus for long times, cross-shore dispersion induced by vortical motions appears to dominate over breaking wave (bore) induced dispersion.

[41] For the asymptotic alongshore diffusivity  $\hat{\kappa}_{yy}^\infty$ , two scalings are investigated: one based on dimensional considerations and mixing-length arguments [Tennekes and Lumley, 1972] and another related to shear dispersion in a pipe [Taylor, 1953]. The mixing-length  $\hat{\kappa}_{yy}^\infty$  scaling uses the mean alongshore current maximum  $\bar{v}_m$  (Table 1) for the velocity scale as  $\bar{v}_m$  is related to the fluctuating (shear wave) velocity [Noyes et al., 2004]. Using the surfzone width  $L_{sz}$  as a length-scale (see Table 1) yields

$$\hat{\kappa}_{yy}^\infty \simeq \gamma |\bar{v}_m| L_{sz} \quad (18)$$

with  $\gamma$  a nondimensional constant of proportionality. Fitting the HB06 observations to equation (18) results in best fit  $\gamma = 0.52 \pm 0.08$  with skill of 0.68 (Figure 9a). The surfzone width  $L_{sz}$  varied little thus fit skill with constant length scale is also similar. TP04 day one  $\hat{\kappa}_{yy}^\infty$  follows the scaling (18), whereas day two with the larger mean current does not.

[42] Shear dispersion in a pipe (three dimensional [Taylor, 1953]), adapted to a simple two-dimensional parabolic alongshore current [Spydell et al., 2007], yields

$$\hat{\kappa}_{yy}^\infty = \frac{\bar{v}_m^2 L^2}{480 \kappa_{xx}^{\text{pipe}}}, \quad (19)$$

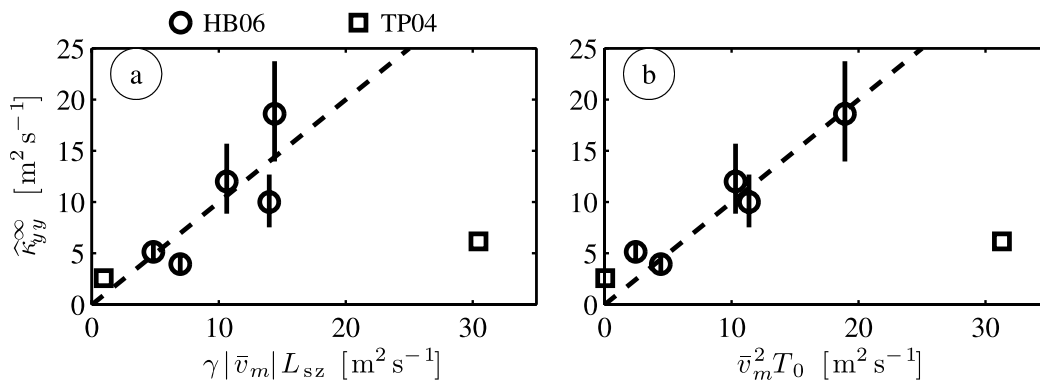


**Figure 9.** The HB06 asymptotic alongshore diffusivity  $\hat{\kappa}_{yy}^\infty$  (circles) versus (a)  $\gamma |\bar{v}_m| L_{sz}$  and (b)  $\bar{v}_m^2 T_0$ . The best fit, constrained to go through the origin (dashed lines), results in (a)  $\gamma = 0.52 \pm 0.08$  with a 0.68 skill and (b)  $T_0 = 154 \pm 13 \text{ s}$  with a 0.91 skill. The maximum alongshore current  $\bar{v}_m$  excludes sensors 1 and 2, which are close to the shoreline and/or out of the water. Vertical lines indicate  $\hat{\kappa}_{yy}^\infty$  error bars (Appendix D). Also shown (but not included in the fit) are TP04 [Spydell et al., 2007] data points. Due to data limitations, TP04 error bars could not be calculated.

where  $\kappa_{xx}^{pipe}$  is the constant cross-shore *pipe* diffusivity and  $\bar{v} = 0$  at  $x = 0$ ,  $L$  is assumed. Defining a cross-pipe diffusive timescale  $T_0 = L^2 / (480 \kappa_{xx}^{pipe})$ , equation (19) becomes

$$\hat{\kappa}_{yy}^\infty \simeq \bar{v}_m^2 T_0. \quad (20)$$

As  $L_{sz}$  and  $\hat{\kappa}_{xx}^\infty$  were relatively constant on the four days with  $\hat{\kappa}_{xx}^\infty > 0$ ,  $T_0$  is assumed constant. Fitting to equation (20) yields  $T_0 = 154 \pm 13$  s with a fit skill of 0.91 (Figure 9b). Note that for days with  $\hat{\kappa}_{xx}^\infty > 0$ , the values of  $T_0$  and  $\tau_{xx}$  are similar (Table 2). Using a value of  $\hat{\kappa}_{xx}^\infty = 1 \text{ m}^2 \text{ s}^{-1}$  for  $\kappa_{xx}^{pipe}$  and  $L = 150$  m (where  $\bar{v} \approx 0 \text{ m s}^{-1}$ , in Figure 2) results in  $T_0 = 46$  s, 1/3 of the best fit value. Using daily values of  $\hat{\kappa}_{xx}^\infty$  and  $L_{sz}$  for  $\kappa_{xx}^{pipe}$  and  $L$ , respectively in equation (19) and allowing for a fit coefficient, results in slightly less skill than with constant  $T_0$  equation (20). This all indicates that the observed  $\hat{\kappa}_{yy}^\infty$  is largely consistent with the shear dispersion model (19). Differences are potentially due to the violation of shear dispersion scaling assumptions including a constant in time  $\kappa_{xx}$  and uniform cross-shore drifter sampling. In summary, the alongshore diffusivities are consistent with both the mixing length scaling and the shear dispersion scaling.

[43] The shear dispersion scaling (19) has  $\hat{\kappa}_{xx}^\infty \sim \bar{v}_m^2$ , indicating that strong alongshore currents result in large alongshore diffusivity. However, the TP04 day 2 (with large  $\bar{v}_m$ )  $\hat{\kappa}_{yy}^\infty$  is not consistent with either the shear dispersion scaling (20) nor the mixing-length scaling (18) found for HB06 (Figure 9). This inconsistency is perhaps due to relatively poor Lagrangian sampling on TP04 day two which had about half the mean trajectory length and total drifter data of that on each HB06 day. Short drifter trajectories and sparse observations result in large sampling errors (section 4.3.2). It is also possible that the  $\hat{\kappa}_{yy}^\infty$  scalings (18) and (19) do not apply at Torrey Pines. Additional observations, on beaches without bathymetric controls on the circulation, are needed to test the generality of these  $\hat{\kappa}_{yy}^\infty$  scalings.

## 4.2. Displacements

[44] With homogeneous turbulence, the diffusivity  $\kappa$  does not depend on position and displacement pdfs are Gaussian, i.e., the diffusion equation has Gaussian solutions. However, for position dependent diffusivity, Lagrangian statistics are inhomogeneous and displacement pdfs are non-Gaussian in a manner similar to particle separation pdfs in turbulent flows [Richardson, 1926]. Non-Gaussian pdfs may indicate that dispersion is better represented with a spatially dependent diffusivity, than with a single bulk  $\kappa$  as estimated here. The peakier than Gaussian displacement pdfs (Figure 6a at  $t = 30$  s) that correspond to low  $p$  values (Figure 7) may result from drifters sampling regions of cross-shore inhomogeneous statistics. This phenomena has been observed for open ocean studies of velocity pdfs [Gille and Llewellyn Smith, 2000; LaCasce, 2005].

[45] The HB06 drifter trajectories clearly sample regions with cross-shore varying statistics. The standard deviation of 1 s  $r_x$  and  $r_y$  displacements (proportional to  $\text{std}(u)$  and  $\text{std}(v)$  in Figure 2) vary across the surfzone by about a factor of 2.5. Intermediate-time (30 s) displacements have even more cross-shore variation. For example, consider the standard deviation of 30 s displacements  $\sigma(x_i)$  binned by

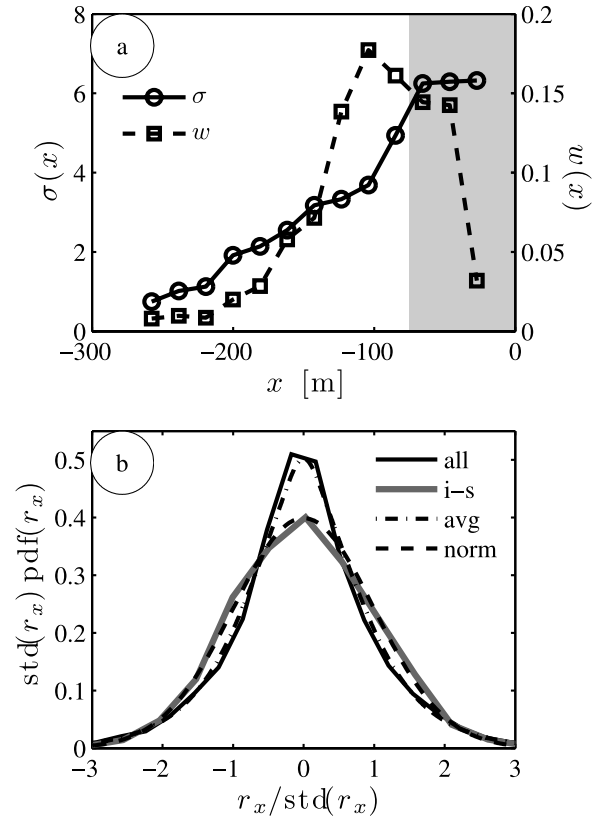


**Figure 10.** (a) On 10/15, standard deviation  $\sigma(x_i)$  (solid curve and circles) of binned 30 s cross-shore displacements  $r_x(30 \text{ s})$  and fractional number of displacements in each bin  $w(x_i)$  (dashed curve and squares) versus the cross-shore position  $x$ . The inner surfzone ( $x > -75$  m) is indicated by shading. (b) The observed normalized probability distribution function of  $r_x(30 \text{ s})$  over all cross-shore bins (solid line) and limited to inner surfzone (denoted by “i-s”) bins (gray thick line). Also shown are  $\bar{P}$  (equation (21), dashed-dot curve) and a normal distribution (dashed curve). To calculate  $\bar{P}$ ,  $N^{(x)} = 13$  and  $n_{\text{tot}} = 70,157$ . The inner surfzone  $n_{\text{tot}} = 22,272$ .

the cross-shore midpoint of the displacement. On 10/15,  $\sigma(x_i)$  increases toward the shore and becomes constant in the inner surfzone ( $x > -75$  m, Figure 10a, shaded region), varying from offshore to onshore by a factor of six (Figure 10a, circles).

[46] This cross-shore variation in  $\sigma(x_i)$  can result in non-Gaussian displacement pdfs. Assume that in the  $i$ th bin, there are  $n_i$  displacements with Gaussian pdf and variance  $\sigma_i^2$ . The average pdf of all  $r_x$  displacements is given by the weighted sum of the Gaussian pdfs over all the bins,

$$\bar{P}(r_x) = \sum_i^{N^{(x)}} \frac{w_i}{\sigma_i \sqrt{2\pi}} \exp\left(-\frac{r_x^2}{2\sigma_i^2}\right), \quad (21)$$

where  $N^{(x)}$  is the total number of bins and the weight  $w_i = n_i/n_{\text{tot}}$  is the fraction of displacements in the  $i$ th bin (Figure 10a, squares).

[47] Using the 30 s displacements standard deviations  $\sigma(x_i)$  and associated weights  $w(x_i)$  in equation (21) results in

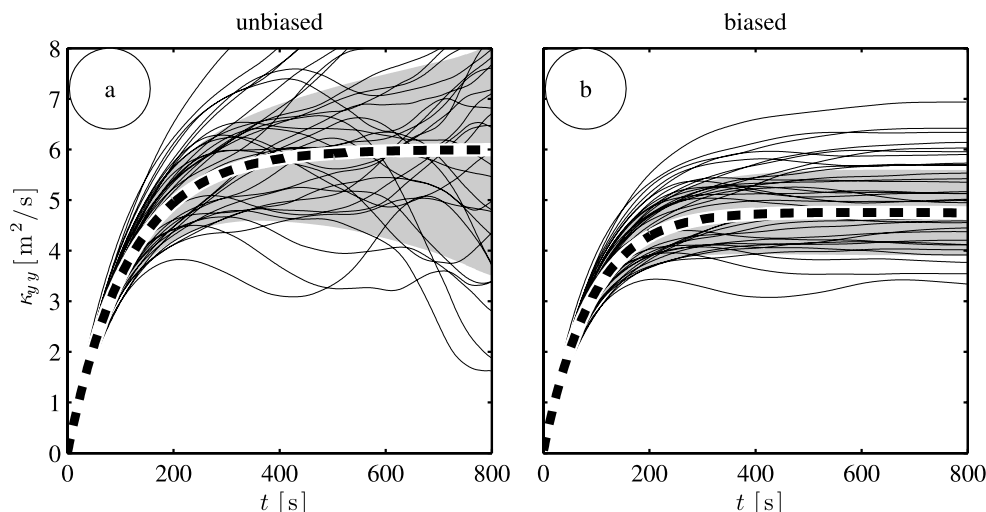


**Figure 11.** Realizations of simulated TP04 day 2 alongshore diffusivity versus time: (a) unbiased  $\kappa_{yy}$  and (b) biased  $\kappa_{yy}^{(B)}$ . There are 36 individual realizations (thin solid lines). The expected diffusivity ( $\bar{\kappa}_{yy}$ ,  $\bar{\kappa}_{yy}^{(B)}$ ) is the thick dashed line with error bars (68% confidence) given by gray shading.

a peakier than a Gaussian pdf  $\bar{P}$  that is similar to the observed 30 s displacement pdf  $P(r_x)$  (Figure 10b, compare solid and dash-dotted), and is clearly different from Gaussian (Figure 10b). Quantitatively, the K-S test  $p$  value between the 30 s displacement pdf and  $\bar{P}$  is 0.97 whereas compared to a Gaussian it is 0.12. For inner surfzone displacements ( $x > -75$  m), 30 s displacement standard deviations  $\sigma(x_i)$  are constant and the inner surfzone (i-s) 30 s displacement pdf  $P_{i-s}$  is approximately Gaussian (Figure 10b, compare gray and dashed curves,  $p$  value of 0.54). Thus displacements in each cross-shore bin appear approximately Gaussian, but when all displacements are lumped into a single bin containing variable statistics, the resulting pdf is non-Gaussian. According to the central limit theorem, the large  $t$  displacement pdfs should be Gaussian as many random displacements that span the entire cross-shore region (with differing statistics) are combined during large  $t$  displacements. For example, all cross-shore displacement pdfs (except 10/15) become more Gaussian for larger times (Figure 7).

[48] For times where the displacements are non-Gaussian,  $\kappa_{xx}(t)$  (and  $\kappa_{yy}(t)$ , not shown) should depend on both cross-shore location and time. However, the present observations cannot resolve such cross-shore variation. Thus the  $\kappa(t)$  reported here is a bulk value representative of the dispersion in the entire surfzone, and should be used cautiously in a Fickian diffusion equation.

#### 4.3. Estimating the Diffusivity: Biases and Sampling Errors

[49] For the TP04 data, biased LVAFs were used to estimate single particle diffusivities (i.e.,  $\kappa_{yy}^{(B)}(t)$ ) since the number of drifter trajectories was small and the drifter trajectory lengths were short [Spydell et al., 2007]. As the alongshore direction is unbounded,  $\kappa_{yy}$  is expected to monotonically increase and eventually asymptote. The relative paucity of TP04 day two data yielded noisy, non-monotonic unbiased  $\kappa_{yy}(t)$ , resulting in unexpectedly small

long-time  $\kappa_{yy}$ . In contrast, the biased  $\kappa_{yy}^{(B)}(t)$  monotonically increased. Thus, Spydell et al. [2007] reported biased LVAF based  $\kappa_{yy}^{(B)}(t)$ .

[50] The pros and cons of using a biased LVAF based  $\kappa_{yy}^{(B)}$  rather than an unbiased LVAF based  $\kappa$  are illustrated with the following example (Figure 11). Realizations of TP04 day two unbiased  $\kappa_{yy}(t)$  and biased  $\kappa_{yy}^{(B)}(t)$  were calculated from simulated drifter trajectories from a first-order autoregressive process with  $\kappa_{yy}^{\infty} = 6 \text{ m}^2 \text{ s}^{-1}$  and  $\tau_{yy} = 115$  s. A single realization is constructed from  $n_0 = 72$  trajectories with mean length ( $\pm$ standard deviation)  $T = 565$  ( $\pm 186$ ) s, giving a nondimensional mean trajectory length  $\tilde{T} = T/\tau_{yy} \approx 5$ . Each realization represents the  $\kappa_{yy}(t)$  and  $\kappa_{yy}^{(B)}(t)$  that would be estimated from a realization of drifter releases.

[51] Due to short trajectories relative to  $\tau_{yy}$  ( $\tilde{T} \approx 5$ ) and small  $n_0$ , the unbiased  $\kappa_{yy}$  realizations have significant sampling error and are considerably spread about the expected (true)  $\bar{\kappa}_{yy}(t)$ , particularly at  $t > 2\tau_{yy}$  (Figure 11, compare solid thin and dashed thick curves). Increasing  $n_0$  or  $T$  reduces the scatter in the  $\kappa_{yy}$  realizations. Corresponding biased  $\kappa_{yy}^{(B)}$  realizations have a mean error and underpredict the expected  $\bar{\kappa}_{yy}(t)$ . However, they are more stable and have less scatter about the expected biased value  $\bar{\kappa}_{yy}^{(B)}$  (Figure 11b, compare solid thin lines and solid thick line). Due to sampling error, some long-time unbiased  $\kappa_{yy}$  realizations are smaller than all biased  $\kappa_{yy}^{(B)}$  realizations. Thus at times approaching the trajectory length, uncertainties in the long-time unbiased  $\kappa_{yy}$  may warrant use of the biased diffusivities. The tradeoffs of using an unbiased (larger sampling error) or biased (larger mean error)  $\kappa$  are considered.

##### 4.3.1. Biased Diffusivity Mean Error

[52] The difference between expected unbiased  $\bar{\kappa}(t)$  and biased  $\bar{\kappa}_{yy}^{(B)}(t)$  can be significant (Figures 11a and 11b, compare dashed thick lines) where  $\kappa_{yy}^{(B)}$  has a mean error and underestimates the true expected  $\bar{\kappa}_{yy}$ . The mean error magnitude is a function of trajectory length. From trajectory-

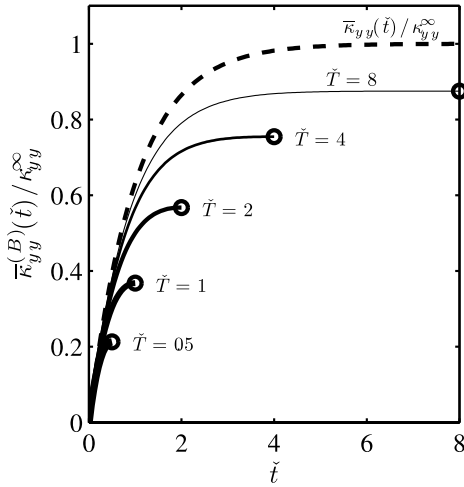


**Figure 12.** Expected biased to asymptotic alongshore diffusivity ratio  $\bar{\kappa}_{yy}^{(B)}/\kappa_{yy}^{\infty}$  versus normalized time  $\tilde{t} = t/\tau_{yy}$  for varying trajectory lengths  $\tilde{T}$  (see line labels). The dashed curve represents the expected unbiased to asymptotic alongshore diffusivity  $\bar{\kappa}_{yy}(\tilde{t})/\kappa_{yy}^{\infty}$ .

ries of equal length  $T$ , the unbiased and biased alongshore LVAFs are

$$C_{yy}(t) = \frac{1}{T-t} \int_0^{T-t} v(a)v(a+t) da$$

$$C_{yy}^{(B)}(t) = \frac{1}{T} \int_0^{T-t} v(a)v(a+t) da$$

respectively. The  $C_{yy}^{(B)}$  denominator uses the full trajectory length  $T$  whereas  $C_{yy}$  uses  $T-t$ , the number of observations at each  $t$ , which decrease with  $t$ . Using (equation (7)), the corresponding nondimensionalized analytic LVAFs are

$$\tilde{C}_{yy}(\tilde{t}) = \exp(-\tilde{t}) \quad \text{and}$$

$$\tilde{C}_{yy}^{(B)}(\tilde{t}) = (1 - \tilde{t}/\tilde{T}) \exp(-\tilde{t})$$

where  $\tilde{t} = t/\tau_{yy}$ , and  $\tilde{T} = T/\tau_{yy}$  are nondimensional time and trajectory length, respectively. The biased  $\tilde{C}_{yy}^{(B)}$  has an error of  $-\tilde{t} \exp(-\tilde{t})/\tilde{T}$ . Nondimensional expected unbiased and biased diffusivities are

$$\bar{\kappa}_{yy}(\tilde{t}) = (1 - \exp(-\tilde{t}))$$

$$\bar{\kappa}_{yy}^{(B)}(\tilde{t}) = (1 - \exp(-\tilde{t}))(1 - 1/\tilde{T}) + \tilde{t} \exp(-\tilde{t})/\tilde{T}.$$

Expected unbiased and biased  $\bar{\kappa}_{yy}$  differences are largest for  $\tilde{t} \rightarrow \tilde{T}$  (Figure 12). At  $\tilde{t} = \tilde{T}$ , the expected biased diffusivity  $\bar{\kappa}_{yy}^{(B)}(\tilde{t})$  has asymptoted to a maximum. The dimensional  $\bar{\kappa}_{yy}^{(B)}(\tilde{T})$  underestimates  $\kappa_{yy}^{\infty}$  by

$$\frac{\bar{\kappa}_{yy}^{(B)}(\tilde{T})}{\kappa_{yy}^{\infty}} = (1 - 1/\tilde{T}) + \tilde{T} \exp(-\tilde{T}).$$

This mean error is largest for short  $\tilde{T}$  (Figure 12, circles, compare the trajectory end points).

#### 4.3.2. Sampling Errors

[53] Unbiased  $\kappa_{yy}$  sampling errors can obscure the desired long-time diffusivity (e.g., Figure 11a). As the number of observations at each  $t$  decrease with  $t$ , (e.g., for  $n_0 = 1$ , there is only one observation at  $t = T$ ). The unbiased  $\kappa_{yy}$  sampling error increases rapidly with time as  $\tilde{t} \rightarrow \tilde{T}$ . To estimate the increased sampling error versus increased mean error trade-off between an unbiased versus biased  $\kappa_{yy}$ , the unbiased and biased  $\kappa_{yy}$  sampling error dependence upon  $t$  and  $T$  is now examined.

[54] The unbiased  $\kappa_{yy}$  sampling error is

$$\epsilon_{\kappa_{yy}}(t) = \left( E \left\{ [\kappa_{yy}(t) - \bar{\kappa}_{yy}(t)]^2 \right\} \right)^{1/2}$$

where  $E$  is the expectation operator over many realizations such that  $\bar{\kappa}_{yy}(t) = E[\kappa_{yy}(t)]$ . For the analytic LVAF (7),  $\bar{\kappa}_{yy}(\tilde{t}) = 1 - \exp(-\tilde{t})$ . The  $\epsilon_{\kappa_{yy}}$  estimation method for trajectories varying in length  $T$  is complex (Appendix B). However, for  $n_0$  equal length trajectories, the analytic LVAF (7), and nondimensionalizing by  $\tilde{t} = t/\tau_{yy}$  and  $\tilde{T} = T/\tau_{yy}$ , the sampling error simplifies to

$$\frac{\epsilon_{\kappa_{yy}}(\tilde{t})}{\kappa_{yy}^{\infty}} = \begin{cases} [2E_1(\tilde{t})]^{1/2} & \text{for } \tilde{t} \ll 1 \\ [E_1(\tilde{t})]^{1/2} & \text{for } \tilde{t} \gg 1 \end{cases} \quad (22)$$

where

$$E_1(\tilde{t}) = \frac{2}{n_0} \int_0^{\tilde{t}} 1 - \exp(-\tilde{t}') + \frac{\Gamma(0, \tilde{T}) - \Gamma(0, \tilde{T} - \tilde{t}')}{2(\tilde{T} - \tilde{t}')} \\ \times \left\{ \exp(\tilde{T} - \tilde{t}') [2(\tilde{T} - \tilde{t}')^2 - 2(\tilde{T} - \tilde{t}') + 1] \right. \\ \left. - \exp(\tilde{t}' - \tilde{t}') \right\} d\tilde{t}' \quad (23)$$

with  $\Gamma$  the incomplete gamma function. The diffusivity sampling error dependence upon time  $\tilde{t}$  and trajectory length  $\tilde{T}$  is examined for the full estimate (equations (B3) and (B4)), and various limits of equation (22) (Figure 13).

[55] For times much shorter than the Lagrangian time-scale (i.e.,  $\tilde{t} \ll 1$ ),

$$\frac{\epsilon_{\kappa_{yy}}(\tilde{t})}{\kappa_{yy}^{\infty}} \sim \frac{1}{\sqrt{n_0}} (2\tilde{T} + \exp(-2\tilde{T}) - 1)^{1/2} \frac{\tilde{t}}{\tilde{T}}, \quad (24)$$

and the error grows linearly in time (Figure 13). For trajectory lengths  $\tilde{T} \lesssim 5$ , error growth is approximately linear for all  $t$  (see  $\tilde{T} = 1, 5$ , Figures 13a and 13b). For long trajectory lengths with  $\tilde{T} - \tilde{t} \gg 1$ ,

$$\frac{\epsilon_{\kappa_{yy}}(\tilde{t})}{\kappa_{yy}^{\infty}} \sim \frac{2}{\sqrt{n_0}} \left[ \ln \left( \frac{\tilde{T}}{\tilde{T} - \tilde{t}} \right) \right]^{1/2} \quad (25)$$

and grows rapidly as  $\tilde{t} \rightarrow \tilde{T}$  due to the decreasing number of observations (Figure 13b, thick-dashed gray curve). The

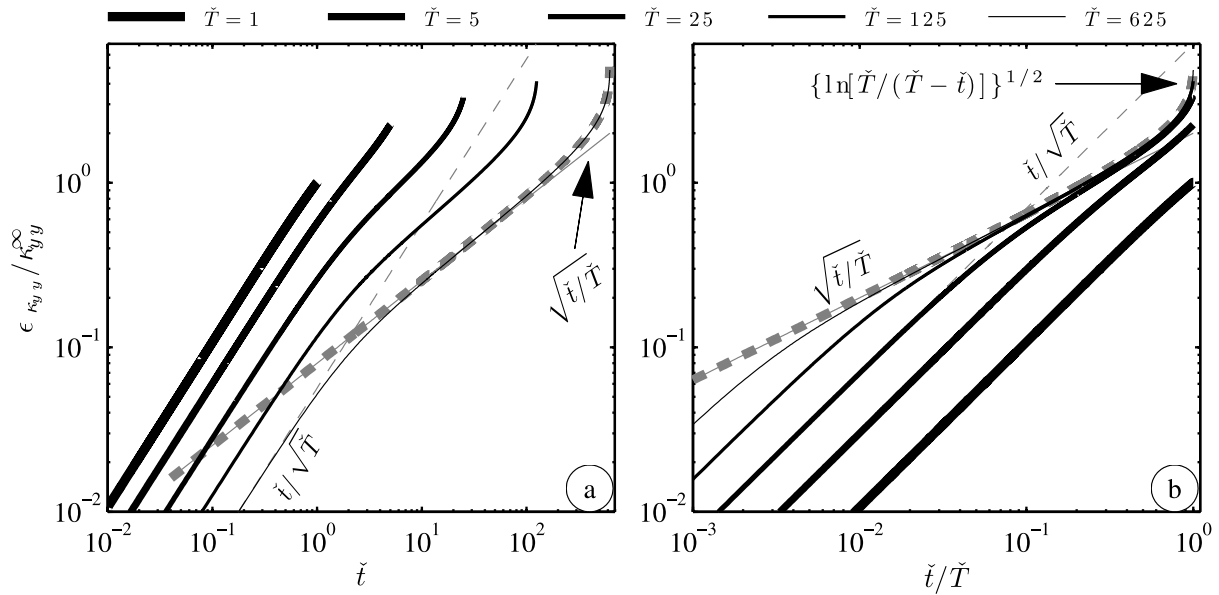


**Figure 13.** Normalized diffusivity sampling error  $\epsilon_{\kappa_{yy}}/\kappa_{yy}^{\infty}$  (from equation (B3)) for one trajectory ( $n_0 = 1$ ) of varying lengths  $\tilde{T}$  (see legend) versus (a)  $\tilde{t} = t/\tau_{yy}$  and (b)  $\tilde{t}/\tilde{T}$ . The scalings derived from  $E_1(t)$  (equation (23)) are shown as gray curves: the short-time scaling  $\epsilon_{\kappa_{yy}} \sim \tilde{t}/\sqrt{\tilde{T}}$  (thin-dashed), the long  $\tilde{T}$  scaling  $\epsilon_{\kappa_{yy}} \sim \{\ln[\tilde{T}/(\tilde{T} - \tilde{t})]\}^{1/2}$  (thick-dashed), and the intermediate scaling  $\epsilon_{\kappa_{yy}} \sim \sqrt{\tilde{t}/\tilde{T}}$  (thin-solid). The rapidly growing portion of the log scaling is only evident for  $\tilde{t}/\tilde{T} \rightarrow 1$ .

singularity at  $\tilde{t} = \tilde{T}$  predicted by equation (25) is not in the full solution (23) which has a small boundary layer correction of unit thickness at  $\tilde{t} = \tilde{T}$ . For  $\tilde{t}/\tilde{T} \ll 1$ , equation (25) reduces to

$$\frac{\epsilon_{\kappa_{yy}}(\tilde{t})}{\kappa_{yy}^{\infty}} \sim \frac{2}{\sqrt{n_0}} \left(\frac{\tilde{t}}{\tilde{T}}\right)^{1/2}, \quad (26)$$

i.e., the  $t^{1/2}$  growth given by Davis [1991]. For diffusivities based on unbiased LVAFs, the  $\tilde{t}^{1/2}$  error growth (equation (26)) only applies for  $\tilde{t}/\tilde{T} < 0.3$  (see Figure 13b). This long-time duration of rapid error growth (equation (25)) is obscured by the logarithmic abscissa in Figures 13a and 13b.

[56] The HB06 drifter mean nondimensional trajectory lengths are  $\tilde{T} \approx 4$ –8 resulting in approximately linear (24) sampling error growth. Using the observed mean trajectory length  $T$  and  $n_0$  in equation (24) results in approximately the full  $\kappa_{yy}$  sampling error (equations (B2)–(B4)) shown in Figure 4b.

[57] Turning now to the biased diffusivity, the variance about the expected biased diffusivity  $\bar{\kappa}_{yy}^{(B)}$  is

$$\sigma_{\kappa_{yy}^{(B)}}(\tilde{t}) = \left( E \left\{ \left[ \kappa_{yy}^{(B)}(\tilde{t}) - \bar{\kappa}_{yy}^{(B)}(\tilde{t}) \right]^2 \right\} \right)^{1/2}$$

( $\pm\sigma_{\kappa_{yy}^{(B)}}$  is the shading in Figure 11b). The small time behavior of  $\sigma_{\kappa_{yy}^{(B)}}(\tilde{t})$  is the same as  $\epsilon_{\kappa_{yy}}(\tilde{t})$  given by equation (24). For long trajectories  $\tilde{T} \gg 1$ ,

$$\frac{\sigma_{\kappa_{yy}^{(B)}}(\tilde{t})}{\kappa_{yy}^{\infty}} \sim \frac{1}{\sqrt{n_0}} \left[ 2 + \frac{\tilde{T} - \tilde{t}}{\tilde{T}^2} - 2 \frac{(\tilde{T} - \tilde{t})^2}{\tilde{T}^2} \right]^{1/2},$$

which is equivalent to equation (26) for small  $\tilde{t}/\tilde{T}$ . Thus both  $\epsilon_{\kappa_{yy}}$  and  $\sigma_{\kappa_{yy}^{(B)}}$  increase like  $\tilde{t}^{1/2}$  for dimensional times much longer than  $\tau_{yy}$  but shorter than the trajectory length  $T$ . The most striking difference between  $\epsilon_{\kappa_{yy}}$  and  $\sigma_{\kappa_{yy}^{(B)}}$  is that  $\sigma_{\kappa_{yy}^{(B)}}$  grows slower than  $\tilde{t}^{1/2}$  and approaches a constant as  $\tilde{t} \rightarrow \tilde{T}$ . This makes individual  $\kappa_{yy}^{(B)}$  realizations more stable at long times and is the main reason that biased diffusivity estimates might be preferred to unbiased. However, the choice of a biased or unbiased diffusivity depends not on  $\sigma_{\kappa_{yy}^{(B)}}(\tilde{t})$  but on the full biased diffusivity sampling error  $\epsilon_{\kappa_{yy}^{(B)}}$ , which includes contributions %This error includes contributions from the variance and the mean error, i.e.,

$$\epsilon_{\kappa_{yy}^{(B)}}(\tilde{t}) = \left\{ \sigma_{\kappa_{yy}^{(B)}}^2(\tilde{t}) + \Delta^2(\tilde{t}) \right\}^{1/2}.$$

where the mean error is

$$\Delta(\tilde{t}) = \bar{\kappa}_{yy}(\tilde{t}) - \bar{\kappa}_{yy}^{(B)}(\tilde{t}).$$

Both  $\epsilon_{\kappa_{yy}}$  and  $\sigma_{\kappa_{yy}^{(B)}}$  parametrically depend upon  $n_0$  and  $T$ , whereas  $\Delta$  depends only upon  $T$ .

### 4.3.3. Comparing Biased and Unbiased Diffusivity Sampling Error

[58] Whether to use the biased or unbiased diffusivity estimates ultimately depends upon the ratio  $\epsilon_{\kappa_{yy}}/\epsilon_{\kappa_{yy}^{(B)}}$ . The time-dependence of  $\epsilon_{\kappa_{yy}}/\epsilon_{\kappa_{yy}^{(B)}}$  as a function of  $n_0$  and  $T$  is examined. With a constant  $n_0 = 72$ ,  $\epsilon_{\kappa_{yy}} < \epsilon_{\kappa_{yy}^{(B)}}$  at all times for short trajectories  $\tilde{T} \leq 4$  (Figure 14a), due to large mean error  $\Delta$ . However, for  $\tilde{T} \geq 8$ ,  $\epsilon_{\kappa_{yy}} > \epsilon_{\kappa_{yy}^{(B)}}$  for  $\tilde{t} > 5$  due to smaller  $\Delta$ , quickly growing  $\epsilon_{\kappa_{yy}}$  and relatively constant  $\epsilon_{\kappa_{yy}^{(B)}}$ .

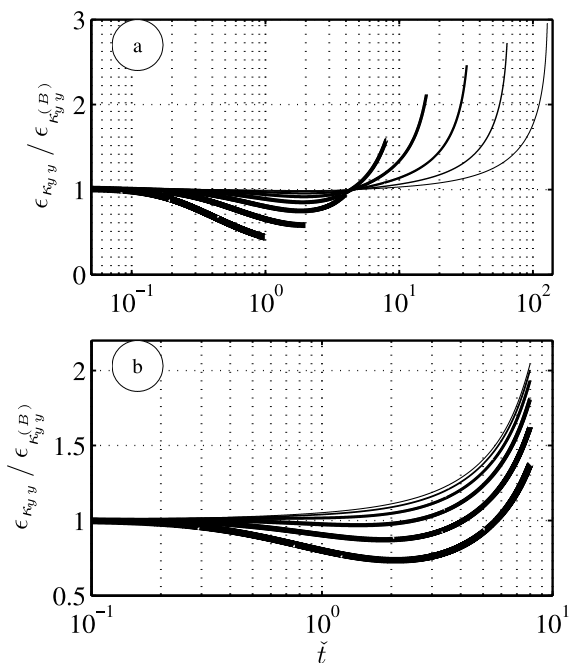


**Figure 14.** The ratio of the unbiased to biased diffusivity sampling error  $\epsilon_{\kappa_{yy}}/\epsilon_{\kappa_{yy}}^{(B)}$  versus nondimensional time  $\tilde{t}$ . (a) The number of drifter trajectories is fixed at  $n = 72$ , and drifter trajectory length is varied  $\tilde{T} = [1, 2, 4, 8, 16, 32, 64, 128]$  indicated by line thickness: the thickest line is the shortest trajectory. (b) Drifter trajectory length is fixed  $\tilde{T} = 8$ , and the number of trajectories is varied  $n_0 = [4, 8, 16, 32, 64, 128]$ , indicated by line thickness: the thickest line is the most trajectories. Note, both axes limits are different in Figures 14a and 14b.

as  $\tilde{t} \rightarrow \tilde{T}$  (Figure 14a). With a constant trajectory length of  $\tilde{T} = 8$ ,  $\epsilon_{\kappa_{yy}} > \epsilon_{\kappa_{yy}}^{(B)}$  for all  $\tilde{t}$  for a small number of trajectories ( $n_0 = 16$ ), whereas for more trajectories  $\epsilon_{\kappa_{yy}} > \epsilon_{\kappa_{yy}}^{(B)}$  only for  $\tilde{t} \rightarrow \tilde{T}$  (Figure 14b). In other words, for sufficient trajectories longer than  $\tau_{yy}$ , so that  $\kappa_{yy}^{\infty}$  is likely approached,  $\epsilon_{\kappa_{yy}}^{(B)} > \epsilon_{\kappa_{yy}}$  and the unbiased diffusivity estimate is better than the biased except for times approaching the trajectory length ( $t \rightarrow T$ ). Given a priori knowledge of the Lagrangian timescale, the number of drifters (or trajectories), and the acceptable level of sampling error, drifter deployment schemes can be designed to meet these criteria.

## 5. Summary

[59] Surfzone dispersion is described with single-particle Lagrangian statistics of GPS-tracked drifters deployed at Huntington Beach Ca over five days with small variation in incident wave height. On each day, ten drifters were repeatedly deployed in the surfzone for 15–30 min. Drifter tracks revealed the presence of alongshore currents (up to 0.35) and low frequency eddies.

[60] Bulk (representative of entire surfzone) Lagrangian velocity autocovariance functions (LVAFs) were used to estimate diffusivities  $\kappa$  (the integral of the LVAF) and dispersions  $D^2$  (the integral of  $\kappa$ ) on each day. The time-

dependent surfzone cross-shore diffusivity  $\kappa_{xx}(t)$  was similar on all days, reaching a local maxima of about  $1.5 \text{ m}^2 \text{ s}^{-1}$  at times 160–300 s before slowly decreasing to about  $1 \text{ m}^2 \text{ s}^{-1}$ . The alongshore diffusivity  $\kappa_{yy}(t)$  increases monotonically for all time  $t$ , following a ballistic scaling at short times. Trajectories were not long enough to observe alongshore Brownian dispersion. For  $t > 50$  s, the alongshore diffusivity  $\kappa_{yy} > \kappa_{xx}$ , consistent with previous observations [Spydell *et al.*, 2007]. Drifters allowed to drift much longer than the present  $O(1000)$  s would eventually be subject to inner-shelf or oceanic processes with different Lagrangian statistics.

[61] The observed diffusivities are well fit by analytic functions, from which asymptotic diffusivities and Lagrangian timescales, representative of the entire surfzone, are determined. The cross-shore asymptotic diffusivity ranged from  $0.53 \leq \hat{\kappa}_{xx}^{\infty} \leq 1.64 \text{ m}^2 \text{ s}^{-1}$ . For the four days with positive values. The asymptotic alongshore diffusivities were  $4 \leq \hat{\kappa}_{yy}^{\infty} \leq 19 \text{ m}^2 \text{ s}^{-1}$ , a much larger range than previously observed [Spydell *et al.*, 2007]. The analytic LVAF e-folding time  $\tau$  is generally  $O(100 \text{ s})$  with the alongshore  $\tau_{yy}$  greater than the cross-shore  $\tau_{xx}$ . The cross-shore Lagrangian timescale is shorter than  $\tau_{xx}$  due to the nonmonotonic  $\kappa_{xx}$  time dependence. Thus asymptotic diffusion is apparent sooner in the cross-shore than in the alongshore. The asymptotic cross-shore diffusivity  $\hat{\kappa}_{xx}^{\infty}$  was not well fit by a previously proposed parameterization based upon the incident wave height and wave period, although the wave height and  $\hat{\kappa}_{xx}^{\infty}$  variability was weak. The asymptotic alongshore diffusivity  $\hat{\kappa}_{yy}^{\infty}$  is related to the maximum mean alongshore current  $\bar{v}_m$  in a manner consistent with both a mixing-length ( $\sim \bar{v}_m$ ) and a shear dispersion based ( $\sim \bar{v}_m^2$ ) scaling.

[62] The Kolmogorov-Smirnov test shows that the probability density function (pdf) of short-time displacements ( $\lesssim 20 \text{ s}$ ) is nearly Gaussian. Displacement pdfs then become peakier than Gaussian around  $t \approx 30 \text{ s}$ , often followed by a return to Gaussian for long time. This pdf peakiness results from cross-shore variability in displacement statistics and is an indication of cross-shore-dependent diffusivity. Cross-shore diffusivity variation is not resolvable with the present data set. Thus the dispersion statistics presented are representative of the entire surfzone and should be used cautiously in surfzone Fickian diffusion equations.

[63] Differences in unbiased and biased diffusivity estimates using the analytic LVAFs were investigated. The biased diffusivity mean error depends upon the ratio of the trajectory length to the Lagrangian timescale. Both the unbiased diffusivity sampling error  $\epsilon_{\kappa}(t)$ , and the standard deviation of biased diffusivity estimates  $\sigma_{\kappa}^{(B)}(t)$ , depend upon the number of trajectories and the trajectory length. For trajectories of varying lengths the formulae are complicated. However, for equal length trajectories, asymptotic regimes were identified to aid error analysis. For trajectories short relative to the Lagrangian timescale, i.e., for the HB06 deployments, the unbiased sampling error is mostly linear with time. For times approaching the trajectory length, the unbiased sampling error grows rapidly due to the decreasing number of observations. For these long times, the biased diffusivity standard deviation grows much more slowly eventually approaching a constant. The

biased diffusivity sampling error combines the biased diffusivity standard deviation and the mean error. For many trajectories short relative to the Lagrangian timescale, the biased error is larger than the unbiased due to large biased mean errors. For many trajectories longer than the Lagrangian timescale, the unbiased diffusivity estimate is preferred except at times approaching the trajectory length. However, the biased diffusivity may be preferred if there are few but long (compared to the Lagrangian timescale) trajectories.

### Appendix A: Averaging: Using the Entire Trajectory

[64] To calculate statistics of Lagrangian quantities, the averaging method, denoted by  $\langle \cdot \rangle$  in equations such as equations (2) and (4), uses all possible  $t$  separated observations (velocities or positions) along each trajectory. Although the data are discrete, continuous data is assumed for clarity of presentation. Converting to discrete data is straightforward. For drifter trajectories with varying lengths  $T_i$ , the amount (in units of time) of  $t$  separated observations is

$$\mathbb{N}(t) = \left[ \sum_{i=1}^{n(t)} T_i \right] - n(t)t \quad (\text{A1})$$

where  $n(t)$  is the number of trajectories greater than or equal to  $t$  in length. When discretized,  $\mathbb{N}(t)$  is the number of observations separated by  $t$ . To illustrate, consider two trajectories,  $T_1 = 100$  s and  $T_2 = 200$  s. For  $0 \leq t \leq 100$  s,  $n(t) = 2$  and  $\mathbb{N}(t) = 300 - 2t$ , while for  $100 < t \leq 200$  s,  $n(t) = 1$  and  $\mathbb{N}(t) = 200 - t$ . Using  $C_{xx}$  as an example, averages are given by

$$C_{xx}(t) = \langle u(t)u(0) \rangle = \frac{\sum_{i=1}^{n(t)} \int_0^{T_i-t} u_i(a+t)u_i(a) da}{\mathbb{N}(t)}. \quad (\text{A2})$$

The estimate (A2) is unbiased because the denominator  $\mathbb{N}(t)$  uses the actual number of observations at each  $t$ , whereas a biased estimator uses  $\mathbb{N}(t=0)$  at every  $t$  (see section 4.3.1).

### Appendix B: Sampling Errors of Lagrangian Statistics

[65] Sampling errors for the LVAF and absolute diffusivity are defined. For some quantity  $\zeta(t)$ , the sampling error is

$$e_{\zeta}^2(t) = E \left[ (\zeta(t) - \bar{\zeta}(t))^2 \right], \quad (\text{B1})$$

where  $E[\cdot]$  is the expectation operator and  $\bar{\zeta} = E[\zeta]$ . Substituting the definition of the statistic  $\zeta$  into equation (B1),  $\zeta = 1/(T-t) \int_0^{T-t} u'(a)u'(a+t) da$  for the LVAF (unbiased), and after taking expectations, leads to the LVAF sampling error

$$e_{\bar{C}}^2(t) = \frac{\sum_{i=1}^{n(t)} \mathbb{I}_{i,C}(t_1)}{[\mathbb{N}(t_1)]^2} \quad (\text{B2})$$

where  $n(t)$  is the number of trajectories greater than or equal to  $t$  in length and  $\mathbb{N}$  is given in equation (A1). For each trajectory

$$\mathbb{I}_{i,C}(t) = \int_0^{T_i-t} \int_0^{T_i-t} [C(a-b)]^2 + C(a-b-t)C(a-b+t) da db,$$

where  $C$  is the expected LVAF and the sum is over all  $i$  trajectories longer than  $t$ . Following *Spydell et al.* [2007], but using the unbiased definition of  $C$ , the diffusivity sampling error squared  $e_{\bar{C}}^2(t)$  is

$$e_{\bar{C}}^2(t) = \int_0^t \int_0^t \frac{\sum_{i=1}^{n(t)} \mathbb{I}_{i,C}(t_1, t_2)}{\mathbb{N}(t_1)\mathbb{N}(t_2)} dt_1 dt_2 \quad (\text{B3})$$

with

$$\mathbb{I}_{i,C}(t_1, t_2) = \int_0^{T_i-t_2} \int_0^{T_i-t_1} C(a-b)C(a-b+t_1-t_2) + C(a-b-t_2)C(a-b+t_1) db da \quad (\text{B4})$$

for each drifter trajectory. When calculating the sampling error for the observed LVAF  $\varepsilon_C(t)$  and diffusivity  $\varepsilon_{\kappa}(t)$  (shading in Figures 3 and 4, respectively), the analytic cross- and alongshore LVAF  $\bar{C}$  is used in equations (B2) and (B3) for efficiency as the integrals in  $\mathbb{I}_{i,C}$  and  $\mathbb{I}_{i,\kappa}$  can be analytically determined.

### Appendix C: Nonlinear Least Squares Fit for Diffusivity

[66] The analytic LVAF functions (7) and (9) are found by minimizing the squared misfit of diffusivity residuals

$$R(t) = \kappa_{xx}(t) - \hat{\kappa}_{xx}(\boldsymbol{\beta}, t),$$

integrated over time (see equation (11)). The fit is nonlinear in the best fit coefficients  $\boldsymbol{\beta}$  where the number of coefficients is  $n_{\beta}$ : 3 for the cross shore and 2 for the alongshore. The sampling error covariance matrix for  $\boldsymbol{\beta}_0$  is

$$M_{\boldsymbol{\beta}} = \frac{G_0}{m - n_{\beta}} \text{inv}(Q) \quad (\text{C1})$$

where the  $ij$ th component of  $Q$  is

$$Q_{ij} = \int_0^{T_m} \left( \frac{\partial \hat{\kappa}(\boldsymbol{\beta}, t)}{\partial \beta_i} \Big|_{\boldsymbol{\beta}_0} \right) \left( \frac{\partial \hat{\kappa}(\boldsymbol{\beta}, t)}{\partial \beta_j} \Big|_{\boldsymbol{\beta}_0} \right) dt,$$

$G_0$  is the minimum value of  $G$ , and  $m$  is the number of effective samples used in the fit, estimated with  $m = T_m/T_z$  where  $T_z$  is the first zero ( $\sim 100$  s) of the biased autocorrelation function of residuals  $R(t)$ . The square root (the standard deviation) of the diagonal elements of equation (C1) is the error in the fit coefficients (Table 2).

[67] By Monte Carlo simulation, best fit coefficients (e.g.,  $A_{xx}$ ,  $t_0$ , and  $\tau_{xx}$ ) are used to calculate error bars on asymptotic quantities (e.g.,  $\hat{\kappa}_{xx}^{\infty}$  in equation (12)) derived from them. Best fit coefficients are assumed to be Gaussian

random variables with means equal to the best fit values and covariances  $\mathbf{M}_\beta$  (Table 2). For example, consider the asymptotic cross-shore diffusivity  $\hat{\kappa}_{xx}^\infty$ . Sets of randomly generated  $(A_{xx}, t_0, \tau_{xx})$  are used to calculate  $\hat{\kappa}_{xx}^\infty$  values using equation (12). The mean is  $\hat{\kappa}_{xx}^\infty$  and the standard deviation is the number following the  $\pm$  in Table 2. Fit errors for  $T_{xx}^{(L)}$  and  $\hat{\kappa}_{yy}^\infty$  are calculated similarly.

## Appendix D: Asymptotic Diffusivity Sampling Error

[68] The asymptotic diffusivity  $\hat{\kappa}^\infty$  sampling error is the range of fit  $\hat{\kappa}^\infty$  derived from different realizations of surfzone drifter releases with the same statistics. This range is estimated by performing best fits equation (11) for  $t \leq 1000$  s to  $\kappa_{xx}(t) + \epsilon_{\kappa_{xx}}(t)$  and  $\kappa_{xx}(t) - \epsilon_{\kappa_{xx}}(t)$  resulting in best fit coefficients  $(A_{xx}^{(\pm)}, t_0^{(\pm)}, \tau_{xx}^{(\pm)})$  and  $(A_{xx}^{(-)}, t_0^{(-)}, \tau_{xx}^{(-)})$ , respectively. These fit coefficients yield the upper and lower limits of the asymptotic diffusivity sampling error, i.e.,

$$\hat{\kappa}_{xx}^{\infty(\pm)} = A_{xx}^{(\pm)} \tau_{xx}^{(\pm)} \left( 1 - \tau_{xx}^{(\pm)} / t_0^{(\pm)} \right).$$

where

$$\hat{\kappa}_{xx}^{\infty(-)} \leq \hat{\kappa}_{xx}^\infty \leq \hat{\kappa}_{xx}^{\infty(+)}$$

with approximately 68% probability. The alongshore asymptotic diffusivity sampling error is calculated similarly. The  $\hat{\kappa}^\infty$  ranges are given in Table 2 and shown in Figures 8 and 9 as vertical lines.

[69] **Acknowledgments.** CA Coastal Conservancy, NOAA, NSF, ONR, and CA Sea grant. We thank the staff and students from the Integrative Oceanography Division (B. Woodward, B. Boyd, K. Smith, D. Darnell, I. Nagy, D. Clark, M. Omand, M. Yates, M. McKenna, M. Rippey, S. Henderson) for acquiring the field observations for this research.

## References

- Boehm, A., D. Keymer, and G. Shellenbarger (2005), An analytical model of enterococci inactivation, grazing, and transport in the surf zone of a marine beach, *Water Res.*, *39*(15), 3565–3578.
- Brown, J., J. H. MacMahan, A. Reniers, and E. Thornton (2009), Surfzone diffusivity on a rip channel beach, *J. Geophys. Res.*, doi:10.1029/2008JC005153, in press.
- Clarke, L., D. Ackerman, and J. Largier (2007), Dye dispersion in the surfzone: Measurements and simple models, *Cont. Shelf Res.*, *27*, 650–669.
- Davis, R. E. (1987), Modeling eddy transport of passive tracers, *J. Mar. Res.*, *45*, 635–665.
- Davis, R. E. (1991), Observing the general circulation with floats, *Deep Sea Res.*, *38*, S531–S571.
- Dever, E. P., M. C. Hendershott, and C. D. Winant (1998), Statistical aspects of surface drifter observations of circulation in the Santa Barbara Channel, *J. Geophys. Res.*, *103*, 24,781–24,797.
- Dorfman, M., and K. S. Rossetol (2008), Testing the waters: A guide to water quality at vacation beaches, technical report, Natural Resources Defense Council, Cumberland, R. I.
- Feddersen, F. (2007), Breaking wave induced cross-shore tracer dispersion in the surfzone: Model results and scalings, *J. Geophys. Res.*, *112*, C09012, doi:10.1029/2006JC004006.
- Gille, S. T., and S. G. Llewellyn Smith (2000), Velocity probability density functions from altimetry, *J. Phys. Ocean.*, *30*, 125–136.
- Grant, S., J. Kim, B. Jones, S. Jenkins, and J. Wasyl (2005), Surf zone entrainment, along-shore transport, and human health implications of pollution from tidal outlets, *J. Geophys. Res.*, *110*, C10025, doi:10.1029/2004JC002401.
- Harris, T., J. Jordaan, W. McMurray, C. Verwey, and F. Anderson (1963), Mixing in the surf zone, *Int. J. Air Water Pollut.*, *7*, 649–667.
- Henderson, S. M. (2007), Comment on “Breaking wave induced cross-shore tracer dispersion in the surfzone: Model results and scalings”, *J. Geophys. Res.*, *112*, C11005, doi:10.1029/2007JC004378.
- Inman, D., R. Tait, and C. Nordstrom (1971), Mixing in the surfzone, *J. Geophys. Res.*, *26*, 3493–3514.
- Jiang, S. C., and W. Chu (2004), PCR detection of pathogenic viruses in Southern California urban rivers, *Appl. Microbiol. J.*, *97*, 17–28.
- Johnson, D., and C. Pattiaratchi (2004), Transient rip currents and nearshore circulation on a swell-dominated beach, *J. Geophys. Res.*, *109*, C02026, doi:10.1029/2003JC001798.
- Johnson, D., and C. Pattiaratchi (2006), Boussinesq modelling of transient rip currents, *Coastal Eng.*, *53*(5), 419–439.
- LaCasce, J. H. (2005), Eulerian and Lagrangian velocity distributions in the north atlantic, *J. Phys. Ocean.*, *35*, 2327–2336.
- LaCasce, J. H. (2008), Statistics from Lagrangian observations, *Prog. Oceanogr.*, *77*(1), 1–29, doi:10.1016/j.poc.2008.02.002.
- Lumpkin, R., A. Treguier, and K. Speer (2002), Lagrangian eddy scales in the Northern Atlantic Ocean, *J. Phys. Ocean.*, *32*, 2425–2440.
- Mordant, N., J. Delour, E. Lveque, O. Michel, A. Arnodo, and J.-F. Pinton (2003), Lagrangian velocity fluctuations in fully developed turbulence: Scaling, intermittency, and dynamics, *J. Stat. Phys.*, *113*(5/6), 701–717.
- Noyes, T. J., R. T. Guza, S. Elgar, and T. H. C. Herbers (2004), Field observations of shear waves in the surf zone, *J. Geophys. Res.*, *109*, C01031, doi:10.1029/2002JC001761.
- Oltman-Shay, J., P. A. Howd, and W. A. Birkemeier (1989), Shear instabilities of the mean longshore current: 2. Field observations, *J. Geophys. Res.*, *94*, 18,031–18,042.
- Pasquero, C., A. Provenzale, and A. Babiano (2001), Parameterization of dispersion in two-dimensional turbulence, *J. Fluid Mech.*, *439*, 279–303, doi:10.1017/S0022112001004499.
- Peregrine, D. (1998), Surf zone currents, *Theor. Comput. Fluid Dyn.*, *10*, 295–309.
- Reeves, R. L., S. B. Grant, R. D. Mrse, C. M. C. Oancea, B. F. Sanders, and A. B. Boehm (2004), Scaling and management of fecal indicator bacteria in runoff from a coastal urban watershed in Southern California, *Environ. Sci. Technol.*, *38*, 2637–2648.
- Richardson, L. F. (1926), Atmospheric diffusion shown on a distance-neighbour graph, *Proc. R. Soc. A*, *110*, 709–737.
- Ruessink, B. G., J. R. Miles, F. Feddersen, R. T. Guza, and S. Elgar (2001), Modeling the alongshore current on barred beaches, *J. Geophys. Res.*, *106*, 22,451–22,463.
- Schmidt, W. E., B. T. Woodward, K. S. Millikan, and R. T. Guza (2003), A GPS-tracked surf zone drifter, *J. Atmos. Ocean. Technol.*, *20*, 1069–1075.
- Schmidt, W., R. Guza, and D. Slinn (2005), Surf zone currents over irregular bathymetry: Drifter observations and numerical simulations, *J. Geophys. Res.*, *110*, C12015, doi:10.1029/2004JC002421.
- Spydell, M. S., and F. Feddersen (2009), Lagrangian drifter dispersion in the surfzone: Directionally-spread normally incident waves, *J. Phys. Ocean.*, *39*, 809–830.
- Spydell, M., F. Feddersen, R. T. Guza, and W. E. Schmidt (2007), Observing surfzone dispersion with drifters, *J. Phys. Ocean.*, *37*, 2920–2939.
- Swenson, M. S., and P. P. Niller (1996), Statistical analysis of the surface circulation of the California Current, *J. Geophys. Res.*, *101*, 22,631–22,645.
- Taylor, G. I. (1921), Diffusion by continuous movements, *Proc. London Math. Soc.*, *20*, 196–212.
- Taylor, G. I. (1953), Dispersion of soluble matter in solvent flowing slowly through a tube, *Proc. R. Soc. A*, *219*, 186–203.
- Tennekes, H., and J. L. Lumley (1972), *A First Course in Turbulence*, MIT Press, Cambridge, Mass.
- Yeung, P., and S. Pope (1989), Lagrangian statistics from direct numerical simulations of isotropic turbulence, *J. Fluid Mech.*, *207*, 531–586.

F. Feddersen, R. T. Guza, and M. S. Spydell, Integrative Oceanography Division, Scripps Institution of Oceanography, University of California San Diego, 9500 Gilman Drive, La Jolla, CA 92093-0209, USA. (falk@coast.ucsd.edu; rguza@ucsd.edu; mspydell@ucsd.edu)